The Astrophysical Journal, 927:38 (25pp), 2022 March 1 https://doi.org/10.3847/1538-4357/ac4887


# Atmospheric Dynamics of Temperate Sub-Neptunes. I. Dry Dynamics

Hamish Innes and Raymond T. Pierrehumbert
Atmospheric, Oceanic and Planetary Physics, University of Oxford, UK
*Received 2021 September 10; revised 2021 December 9; accepted 2021 December 20; published 2022 March 3*

## Abstract

Sub-Neptunes (planets with radii between 2 and 4 $R_\oplus$) are abundant around M-dwarf stars, yet the atmospheric dynamics of these planets is relatively unexplored. In this paper, we aim to provide a basic underpinning of the dry dynamics of general low-mean-molecular-weight, temperate sub-Neptune atmospheres. We use the ExoFMS general circulation model (GCM) with an idealized gray-gas radiation scheme to simulate planetary atmospheres with different levels of instellation and rotation rates, using the atmosphere of K2-18b as our control. We find that the atmospheres of tidally locked (TL), temperate sub-Neptunes have weak horizontal temperature gradients owing to their slow rotation rates and hydrogen-dominated composition. The zonal wind structure is dominated by high-latitude cyclostrophic jets driven by the conservation of angular momentum. At low pressures we observe superrotating equatorial jets, which we propose are driven by a Rossby–Kelvin instability similar to the type seen in simulations of idealized atmospheres with axisymmetric forcing. By viewing the flow in TL coordinates, we find the predominant overturning circulation to be between the day side and night side, and we derive scaling relations linking the TL stream function and vertical velocities to instellation. Comparing our results to the only other GCM study of K2-18b, we find significant qualitative differences in dynamics, highlighting the need for further collaboration and investigation into the effects of different dynamical cores and physical parameterizations. This paper provides a baseline for studying the dry dynamics of temperate sub-Neptunes, which will be built on in part II with the introduction of moist effects.

*Unified Astronomy Thesaurus concepts:* Exoplanet atmospheres (487); Mini Neptunes (1063); Atmospheric circulation (112)

## 1. Introduction

### 1.1. Sub-Neptunes

In the last decade there has been an explosion in the number of exoplanets discovered with no solar system analog in terms of radius. Before the Kepler mission, 86% of confirmed exoplanets had masses larger than Neptune, whereas 85% of Kepler-detected planets had radii smaller than that of Neptune (Batalha 2014). Exoplanets that fall between Earth's (1 $R_\oplus$) and Neptune's ($\approx$4 $R_\oplus$) radius are generally classified as either super-Earths or sub-Neptunes depending on whether their radii lie below or above the radius valley at 1.5–2.0 $R_\oplus$ (Fulton et al. 2017), respectively. Of the 3359 discovered exoplanets with confirmed radii, 1290 (38%) have radius between 2 and 4 $R_\oplus$ (sub-Neptunes) and 1141 (34%) have radius between 1 and 2 $R_\oplus$ (super-Earths), making them by far the most abundant subclasses of exoplanets detected.[1] Subsequent analysis of planetary population statistics suggests that between 30% and 50% of all main-sequence stars host at least one planet within 1–4$R_\oplus$ (Mayor et al. 2008; Petigura et al. 2013; Marcy et al. 2014; Winn & Fabrycky 2015).

Whereas super-Earths are thought to be either bare rocks or have secondary atmospheres derived from non-$H_2$ solids (Kite & Barnett 2020), sub-Neptunes are characterized by thick, primary atmospheres with a likely high proportion of nebular H and He. The paucity of planets with intermediate radii is proposed to be either due to the loss of H/He envelopes through photoevaporation (Lopez & Fortney 2013; Owen & Wu 2013) or core-driven atmospheric loss (Ginzburg et al. 2016; Gupta & Schlichting 2019).

To date, only five sub-Neptune sized planets have had their atmospheres characterized by spectroscopy: GJ 1214b (Kreidberg et al. 2014), HD 97658b (Knutson et al. 2014), K2-18b (Benneke et al. 2019b), GJ 3470b (Benneke et al. 2019a), and HD 3167c (Mikal-Evans et al. 2021). Determining the composition of a sub-Neptune's atmosphere without spectroscopic measurements is extremely difficult because often several different atmospheric and core compositions can explain the same mass and radius measurements (Rogers & Seager 2010; Fortney et al. 2013; Lopez & Fortney 2013). For example, early work on GJ 1214b (Rogers & Seager 2010) demonstrated that three different scenarios for atmospheric origin (in situ accretion of H/He, sublimated ices, and an outgassed atmosphere) could explain the mass–radius data despite leading to widely varying compositions. When spectroscopic analysis was eventually carried out (Bean et al. 2011; Kreidberg et al. 2014), the relatively flat spectrum was attributed to the presence of clouds, which has thwarted further attempts to constrain its constituents. In addition, recent work has shown the importance of interactions between the atmosphere and magma oceans in setting the metallicity of the atmosphere (Kite et al. 2020). The redox state of the magma ocean depends on whether the planet was formed inside or outside the ice line, which then greatly affects the partition of volatiles between the atmosphere and core.

The measurement of K2-18b's spectrum (Tsiaras et al. 2019; Benneke et al. 2019b) was the first such observation for a sub-Neptune with terrestrial-like instellation (estimated at

[1] Data from the NASA Exoplanet Archive, https://exoplanetarchive.ipac.caltech.edu; accessed 2021 May 14.

1368 $Wm^{-2}$). Observations from the Hubble Space Telescope's Wide Field Camera 3 showed a strong absorption feature at 1.4 $\mu$m, which along with retrieved temperature–pressure profiles was put forward as evidence of liquid water. Several studies since have tried to constrain the composition of the atmosphere using self-consistent 1D models that directly simulate radiative transfer, convective processes, and chemistry (Bézard et al. 2020; Madhusudhan et al. 2020; Piette & Madhusudhan 2020; Scheucher et al. 2020; Blain et al. 2021). In Madhusudhan et al. (2020), a range of planetary compositions for K2-18b, which would fit both the observed mass–radius and spectral data, was proposed. These included rocky worlds with a significant Fe/Si core, sub-Neptunes (with a larger icy component), and water worlds, which are majority $H_2O$ by composition. There was a range of valid solutions that claimed a liquid-water surface was possible—however, this has been disputed by Scheucher et al. (2020), who argued that the small-scale height resulting from evaporation of high-mean-molecular-weight water from a surface ocean would flatten spectral features and be inconsistent with observations. In addition, several water world solutions require a significant proportion of the core mass to be water ($\gtrsim$80% by mass), which may be unlikely from formation considerations (Nettelmann et al. 2011). The detection of water is also somewhat disputed, with two recent papers claiming the data are better fit by $CH_4$ absorption (Bézard et al. 2020; Blain et al. 2021). Despite significant variations in the models, most agree that K2-18b's outer atmosphere is at least 80% $H_2$–He by volume and at most 15% $H_2O$.

### 1.2. General Circulation Model Simulations of Sub-Neptunes

Although there have been many general circulation model (GCM) simulations of hot Jupiters (e.g., Showman & Guillot 2002; Rauscher & Menou 2010; Dobbs-Dixon & Agol 2013; Perez-Becker & Showman 2013; Rauscher & Kempton 2014; Showman et al. 2015; Kataria et al. 2016; Komacek & Showman 2016; Mayne et al. 2017; Mendonça 2020) and terrestrial exoplanets (e.g., Yang et al. 2014; Kaspi & Showman 2015; Koll & Abbot 2016; Haqq-Misra et al. 2018; Komacek & Abbot 2019; Hammond et al. 2020; Sergeev et al. 2020), there have been comparatively fewer studies of sub-Neptune atmospheres, with most focused on GJ 1214b. The works of Menou (2012), Zhang & Showman (2017), and Drummond et al. (2018) investigated the effect of varying metallicity on the atmosphere of GJ 1214b and generally agreed in finding that increased metallicity decreases the equatorial jet width and increases the day–night temperature contrast. The effect of clouds on the dynamics and spectra of GJ 1214b has also been probed (Charnay et al. 2015a, 2015b). The atmosphere of GJ 1214b has also been used to test the differences between standard primitive equation GCM models and models that integrate the equations of motion without the traditional, hydrostatic, and shallow approximations (Mayne et al. 2019). For hot sub-Neptunes it was found that including these nonprimitive terms could change the structure of the deep atmosphere and also affect the location of a planet's hot spot. The deep atmosphere on sub-Neptunes also affects the equilibration times of GCMs (Wang & Wordsworth 2020), with equilibration times of $10^4$ to $10^5$ Earth days often required to reach a steady state.

To date, only one published work has studied the atmosphere of K2-18b with a GCM (Charnay et al. 2021). The circulation was found to be dominated by an overturning day–night circulation, which controlled the location of clouds. The cooling required to induce condensation and cloud cover occurred either at the terminators (from radiative cooling) or at the substellar point (from adiabatic cooling on ascent). Which mechanism dominated depended strongly on the size and density of cloud condensation nuclei, as well as the assumed metallicity of the atmosphere.

Although few sub-Neptunes with hydrogen-dominated atmospheres on the threshold of $H_2O$ condensation have been discovered and characterized, they may prove to be common given the abundance of sub-Neptunes and their predicted compositions (Kite & Barnett 2020). This work aims to build an understanding of the dynamical meteorology of such objects. The effect of condensible water vapor on these atmospheres is another area of interest, due to water having a higher mean molecular weight than the background $H_2$–He gas, in contrast to Earth. The consequence of this on convective adjustment has been highlighted (Leconte et al. 2017), but the effect is also likely to be important for global dynamics. We will investigate the effect of latent heating and compositional gradients in sub-Neptune atmospheres in a later paper (part II). This paper establishes a baseline by exploring the dry dynamics of temperate sub-Neptunes.

We describe the model used in our experiments in Section 2, detail the results in Section 3, and discuss their implications in Section 4.

## 2. Model

### 2.1. ExoFMS

The GCM used for this study is ExoFMS, which is based on GFDL's Flexible Modeling System (Lin & Rood 1997; Lin 2004), which uses a finite-volume dynamical core on a cubed-sphere grid with physics modules adapted for exoplanetary study. ExoFMS has been used previously to study the atmospheres of terrestrial exoplanets (Pierrehumbert & Ding 2016; Hammond & Pierrehumbert 2017, 2018; Pierrehumbert & Hammond 2019) and gas giants (Lee et al. 2020, 2021).

The dynamical core solves the primitive equations with a $\sigma-p$ vertical coordinate that follows the contours of constant geopotential on the bottom boundary and transitions into a pure pressure coordinate in the upper atmosphere. In pressure coordinates ($t$, $\lambda$, $\phi$, $p$), the primitive equations are

$$\frac{Du}{Dt} - \frac{uv\tan\phi}{a} - fv = -\frac{1}{a\cos\phi}\frac{\partial\Phi}{\partial\lambda}, \tag{1a}$$

$$\frac{Dv}{Dt} + \frac{u^2\tan\phi}{a} + fu = -\frac{1}{a}\frac{\partial\Phi}{\partial\phi}, \tag{1b}$$

$$\frac{D\theta}{Dt} = \frac{\theta}{c_pT}\dot{Q}, \tag{1c}$$

$$\frac{\partial\Phi}{\partial\ln p} = -RT, \tag{1d}$$

$$\nabla_h\cdot\boldsymbol{u}_h + \frac{\partial\omega}{\partial p} = 0, \tag{1e}$$

where the symbols are defined in Table 1. Equations (1a) and (1b) represent zonal and meridional momentum balance, Equation (1c) the first law of thermodynamics, Equation (1d)

**Table 1**
Symbol Definitions

| Symbol | Meaning |
|---|---|
| $\Phi$ | Geopotential |
| $\boldsymbol{u}_h$ | Horizontal wind vector $(u,v)$ |
| $\nabla_h \cdot$ | Horizontal divergence operator |
| $\omega$ | Pressure velocity |
| $T$ | Temperature |
| $c_p$ | Heat capacity at constant pressure |
| $R$ | Gas constant |
| $a$ | Planetary radius |
| $f$ | Coriolis parameter $=2\Omega \sin\phi$ |
| $\theta$ | Potential temperature $=T(p/p_0)^{R/c_p}$ |
| $\dot{Q}$ | Heating rate per unit mass |

the hydrostatic balance, and Equation (1e) the continuity of mass.

The diabatic heating rate $\dot{Q}$ is largely determined by the radiative transfer scheme. We use a double-gray scheme, where the radiation is split into two bands: short wave (SW) and long wave (LW). The incoming stellar radiation is assumed to be only in the SW band, and we assume the atmosphere only emits in the LW part of the spectrum. The LW and SW opacities ($\kappa_{\rm LW}$ and $\kappa_{\rm SW}$, respectively) define optical depths ($\tau_{\rm LW}$, $\tau_{\rm SW}$) via the relation:

$$\tau_i = \frac{2\kappa_i}{g}\frac{p}{p_0} \quad i \in (\mathrm{SW}, \mathrm{LW}), \tag{2}$$

using the hemi-isotropic closure to approximate the angular dependence of $\tau$ (Pierrehumbert 2010). Here we have ignored any pressure dependence of the two opacities, which is likely to be a false assumption at higher pressures where collisional-induced absorption due to $H_2$ becomes important (and scales as $\rho^2 \sim p^2$ for an isothermal atmosphere). We justify this simplification in Section 2.2. The downward SW flux, $S_-$, and the upward and downward LW fluxes, ($F_+$, $F_-$), are then calculated via

$$S_- = S_0 e^{-\tau_{\rm SW}}, \tag{3}$$

$$F_- = \int_0^{\tau} \sigma T^4(\tau') e^{-(\tau-\tau')} d\tau', \tag{4}$$

$$F_+ = F_{\rm int} e^{-(\tau_\infty - \tau)} + \int_{\tau}^{\tau_\infty} \sigma T^4(\tau') e^{-(\tau'-\tau)} d\tau', \tag{5}$$

where $S_0$ is the instellation, $F_{\rm int}$ is the LW flux radiating upwards from the interior of the planet, and $\sigma$ is the Stefan–Boltzmann constant. At the lower boundary, the internal flux is added as a temperature tendency to the lowest model layer. The upwards flux at the lower boundary is specified as $\sigma T_b^4$, where $T_b$ is the temperature of the lowest model layer. Because our SW opacities correspond to bottom-boundary optical depths that are much greater than unity, we ignore the small fraction of SW flux that penetrates the bottom boundary ($\sim$1 ppm). We note that the incoming SW radiation does have a zenith angle dependence; however, we are ignoring this dependence on the grounds that the direct beam is largely converted to diffuse radiation by scattering in the optically thick section of the atmosphere (this assumption breaks down in the upper atmosphere where the direct beam is not yet scattered). The radiative heating rate is calculated from these fluxes as

$$\dot{Q}_{\rm rad} = g\frac{d}{dp}(F_+ - F_- - S_-). \tag{6}$$

Enthalpy-conserving dry convective adjustment is performed if the vertical temperature gradient $\partial_p T$ exceeds that of the dry adiabat $R/c_p$.

Unless otherwise stated, the model was run with a constant value of the atmospheric mean molecular weight, $\mu$, which sets the value of the gas constant $R$ through $R = R_*/\mu$, where $R_*$ is the universal gas constant, $8.314\,\mathrm{J\,K^{-1}\,mol^{-1}}$. The heat capacity at constant pressure, $c_p$, was then set by assuming the atmosphere behaved as an ideal diatomic gas such that $R/c_p = 2/7$.

### 2.2. Experiment Setup

We use the temperate sub-Neptune K2-18b as our control experiment. K2-18b is the first sub-Neptune with an Earth-like instellation to have its atmosphere characterized by transmission spectroscopy. Its radius (2.61 $R_\oplus$; Cloutier et al. 2019) and mass ($(8.63 \pm 1.35)M_\oplus$; Cloutier et al. 2019) place it close to the peak of the sub-Neptune population density distributions (Owen & Wu 2017), making it an ideal candidate for generalized GCM experiments.

Table 2 describes the parameters for the control run. The two-stream opacity values and mean molecular weight value $\mu$ are taken from a study of the atmosphere of GJ 1214b (Menou 2012). A reasonable fit to the temperature–pressure profile from Scheucher et al. (2020) was found using a column model based on the same radiative transfer scheme (see Figure 1, green curve). The largest discrepancy comes in the deep atmosphere, where the gray-gas solution significantly underestimates the temperature. This is likely due to two main factors. First, as previously mentioned, collisional-induced absorption can increase the LW opacity at the bottom of the atmosphere greatly. However, including an additional opacity proportional to $p$ only increases the high-pressure temperature either if there is a significant internal flux or if SW heating penetrates to the high-pressure region. Estimates of the internal temperature of K2-18b correspond to internal fluxes of around $1\,\mathrm{W\,m^{-2}}$, which is not enough to increase the lower-layer temperatures significantly.

We investigated the effect of adding a term proportional to $p$ in both LW and SW opacities such that the optical depths were of the form

$$\tau = \tau_0\left(f\left(\frac{p}{p_0}\right)^2 + (1-f)\frac{p}{p_0}\right), \tag{7}$$

where $f$ is a constant between 0 and 1. When $f = 0.8$ for the LW band (note we cannot set $f = 1$ for the LW band because this causes diverging temperatures at $p = 0$), we do not see a significant change in the temperature profiles (see purple curve in Figure 1) and the curve is a worse fit to the Scheucher et al. (2020) profile. When $f = 1$ for the SW band, we find the temperature is much hotter at the bottom of the atmosphere, better matching the Scheucher et al. (2020) profile at the bottom boundary. In Appendix A, we show the result of running one of our 6 day period experiments with this altered SW opacity. This experiment produces qualitatively similar

**Table 2**
Control Experiment Parameters

| Parameter | Value | Comment |
|---|---|---|
| | Planetary parameters | |
| $a$ ($R_\oplus$) | 2.61 | Benneke et al. (2019b) |
| Rotation period (Earth days) | 32.9396 | Cloutier et al. (2017) |
| $S_0$ (W m$^{-2}$) | 1368 | Benneke et al. (2019b) |
| $g$ (m s$^{-2}$) | 12.43 | Benneke et al. (2019b) |
| | Atmospheric parameters | |
| $\mu$ (g mol$^{-1}$) | 2.2 | Menou (2012), solar metallicity |
| $R$ (J kg$^{-1}$ K$^{-1}$) | 3779 | Menou (2012), solar metallicity |
| $R/c_p$ | 2/7 | Ideal diatomic gas |
| $c_p$ (J kg$^{-1}$ K$^{-1}$) | $R \times \frac{1}{R/c_p}$ | … |
| $\kappa_{\rm LW}$ (cm$^2$ g$^{-1}$) | $2 \times 10^{-2}$ | Menou (2012), solar metallicity |
| $\kappa_{\rm SW}$ (cm$^2$ g$^{-1}$) | $8 \times 10^{-4}$ | Menou (2012), solar metallicity |
| $T_{\rm int}$ (K) | 70 | Consistent with Blain et al. (2021) and Piette & Madhusudhan (2020) |
| | Numerical parameters | |
| Horizontal grid resolution | C48 | Each side of the cubed sphere has $48 \times 48$ resolution (Putman & Lin 2007) |
| Vertical grid resolution | 50 | … |
| Bottom-boundary reference pressure (Pa) | $1 \times 10^6$ | … |
| Top-boundary pressure (Pa) | 10 | … |
| Experiment run time (Earth days) | 20,000 | … |
| Substellar longitude | 0° | … |
| Dynamical time step (s) | 60–120 | Varied according to numerical stability |

results to our constant-$\kappa$ approach, though we note the magnitude of the zonal winds when using pressure-dependent opacities differs notably.

We found that including a second SW band with a lower optical depth (≈1) was much more effective at heating the lower atmosphere. An experiment run with this modification was found to not affect the dynamics in an appreciable way.

We study the effect of varying the rotation rate by running the experiment with a faster rotation rate with $P = 6$ days. K2-18b is a slow rotator and lies within the "weak temperature gradient" regime of parameter space (Pierrehumbert & Hammond 2019). Therefore, while we expect decreasing the rotation rate to not change the dynamical regime of the atmosphere, increasing the rotation rate could produce interesting changes in the dynamics. We choose $P = 6$ days because this is the rotation rate of TRAPPIST-1e, a planet with a temperate equilibrium temperature of 251 K (Gillon et al. 2016) orbiting an ultracool M star with an effective temperature of 2550 K (Gillon et al. 2016). Most observed M dwarfs have an effective temperature greater than this value (Casagrande et al. 2008; Rajpurohit et al. 2013), so we would expect temperate exoplanets around the majority of M dwarfs to have longer

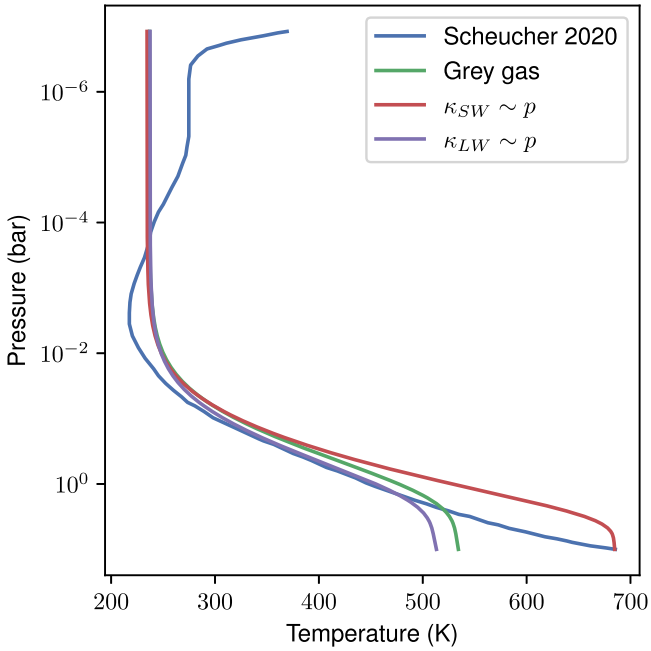


**Figure 1.** Comparison of the radiative equilibrium profile calculated using a simple gray-gas scheme with a correlated-$k$ chemical equilibrium model from Scheucher et al. (2020). We also include profiles calculated with pressure-dependent opacities in the LW (purple curve) and SW (red curve) bands.

**Table 3**
Experiment Setup

| Experiment name | Difference to control |
|---|---|
| PKc | Control experiment (see Table 2) |
| PKh | $S = \frac{1}{2}S_0$ |
| PKd | $S = 2S_0$ |
| P6c | $P = 6$ days |
| P6h | $P = 6$ days, $S = \frac{1}{2}S_0$ |
| P6d | $P = 6$ days, $S = 2S_0$ |

rotation periods than TRAPPIST-1e, making it approximately an upper limit on rotation rate.

We also investigate changing the value of the instellation, running the simulation with $S \in \left\{\frac{1}{2}S_0, S_0, 2S_0\right\}$, where $S_0$ is K2-18b's instellation.

Table 3 summarizes the experiments.

## 3. Results

### 3.1. Convergence

First, we investigate the convergence of the model runs. Figure 2 shows the total kinetic energy of each model run as a function of model day, defined as

$$E_k = \int_A \int_0^{P_s} \frac{dp}{2g}(u^2 + v^2)dA. \quad (8)$$

The kinetic energy of the model runs takes on the order of >15,000 days to reach a steady state (note unless otherwise specified, a "day" is an Earth day, i.e., 86,400 s). With a dynamical time step of 100 s required for stability, the wall-time duration for 1000 days of simulation was between 1–2 days (running the model across 24 CPUs). On the other hand, the maximum and minimum zonal winds of the model reach a steady

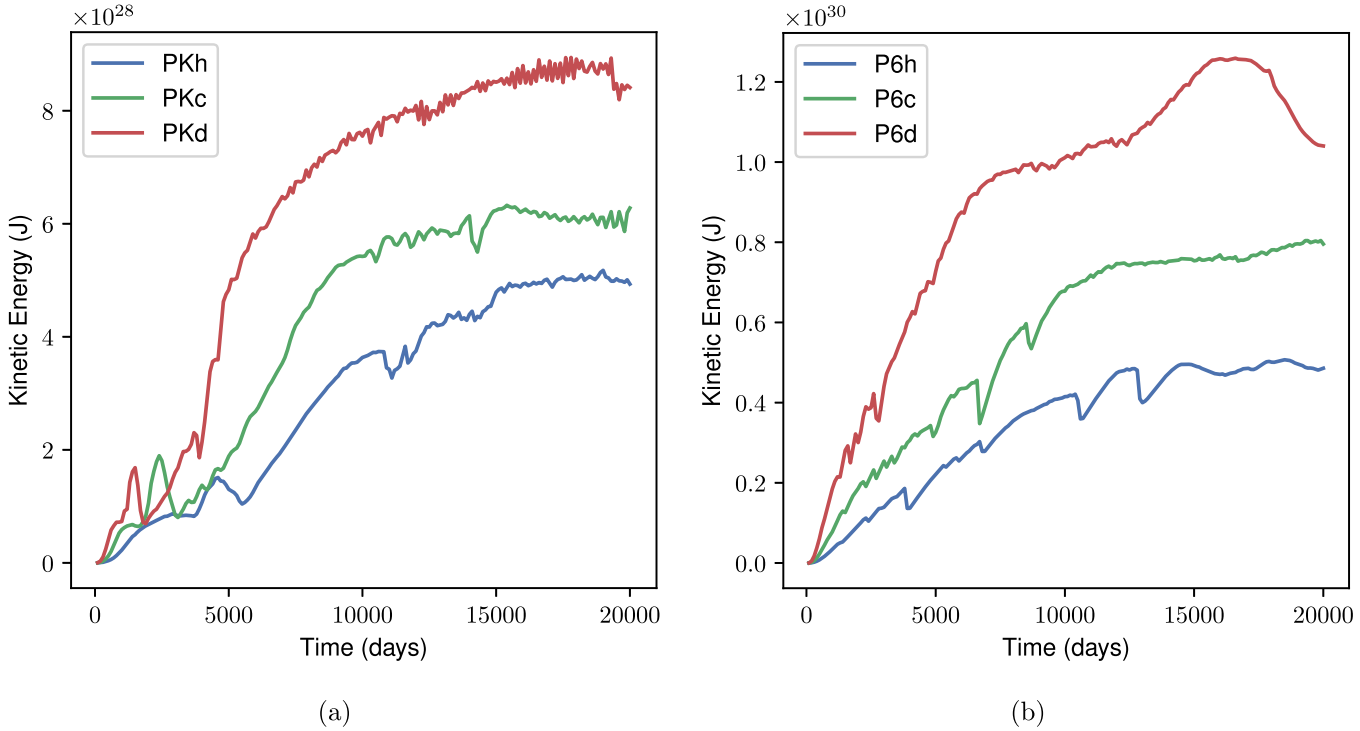


**Figure 2.** The kinetic energy of the dry model runs as a function of model time. (a) The 33 day period runs, with lines indicating different levels of instellation. (b) Equivalent to (a) but with 6 day period runs.

state on day ≈10,000 for the 33 day period runs and <5000 days for the 6 day period runs. While the kinetic energy is dominated by the denser lower atmosphere, the jet speeds are maximal in the upper atmosphere, which takes a shorter period of time to reach its steady state. In the 33 day period experiments, we see the formation of equatorial superrotation in the upper atmosphere only after 10,000 days (see Section 3.5) The globally integrated outgoing LW radiation (OLR) of the model reaches equilibrium with the incoming stellar radiation after ≈1000 days. We see temporal variability of the total kinetic energy even in the equilibrium state. This is caused by fluctuations in the wind field due to the nonlinearity of the equations being solved and also due to the recurrence of instability in the upper atmosphere (see Section 3.5), which results in the variation of the wind field with time. We note that the P6d experiment may not be in equilibrium, with large variations in kinetic energy even at 20,000 days. In Wang & Wordsworth (2020) the convergence of the lower atmosphere took on the order of $10^5$ days, after which the kinetic energy of the atmosphere reached a steady-state value. Our timescale appears to be shorter, which could be attributed to two things: first, our model has a lower bottom-boundary pressure of 10 bar so the radiative timescale will be shorter at the bottom of our model; second, we initialized the simulations with the vertical temperature profile equal to the analytic radiative equilibrium temperature of a 1D gray-gas model. As shown in Section 3.2, because there are extremely weak horizontal temperature gradients throughout the atmosphere, 3D vertical temperature profiles fit the analytic profile well. This would reduce the length of time the lower atmosphere has to adjust to radiative equilibrium (compared to initializing on an isothermal profile, as done in Wang & Wordsworth 2020 and previous studies of GJ 1214b).

### 3.2. Temperature Structure

Figure 3 shows the horizontal temperature structure at 100 mbar. In all plots the substellar point is defined to be at ($\phi$, $\lambda$) = (0°, 0°). The slower-rotating experiments (with $P = 33$ days) show extremely horizontally uniform temperature profiles, with the temperature varying on the order of 1 K apart from near the poles, where there is a more significant drop in temperature in cold, stationary vortex-like structures. In contrast, the faster-rotating experiments show a much larger temperature drop between the equator and pole. The faster-rotating experiments support stronger cyclostrophic jets than the 33 day period experiment (see Sections 3.3 and 3.4), which in turn require a meridional temperature gradient to sustain by gradient-wind balance. The slower-rotating experiments are also less uniform zonally, especially near the poles where there is a region where the meridional and zonal winds are of the same magnitude. In the 6 day period experiments, however, the wind field is extremely zonally uniform at all latitudes. The vertical temperature profiles in all runs closely fit the analytic 1D temperature profile assuming perfect heat redistribution, apart from near the poles. Figure 4 shows vertical temperature profiles at different latitudes and longitudes and in comparison to the 1D analytic solution for the control experiment. Appendix B shows the same data for the rest of the experiments. On the equator, in the zonal direction, there is very little temperature variation. Moving polewards from the substellar point, however, there are significant variations in temperature away from radiative equilibrium. The weak temperature gradients in the tropics and midlatitudes can be explained from a simple scaling argument, following Pierrehumbert & Ding (2016). The momentum equation, written in nondimensionalized form, is

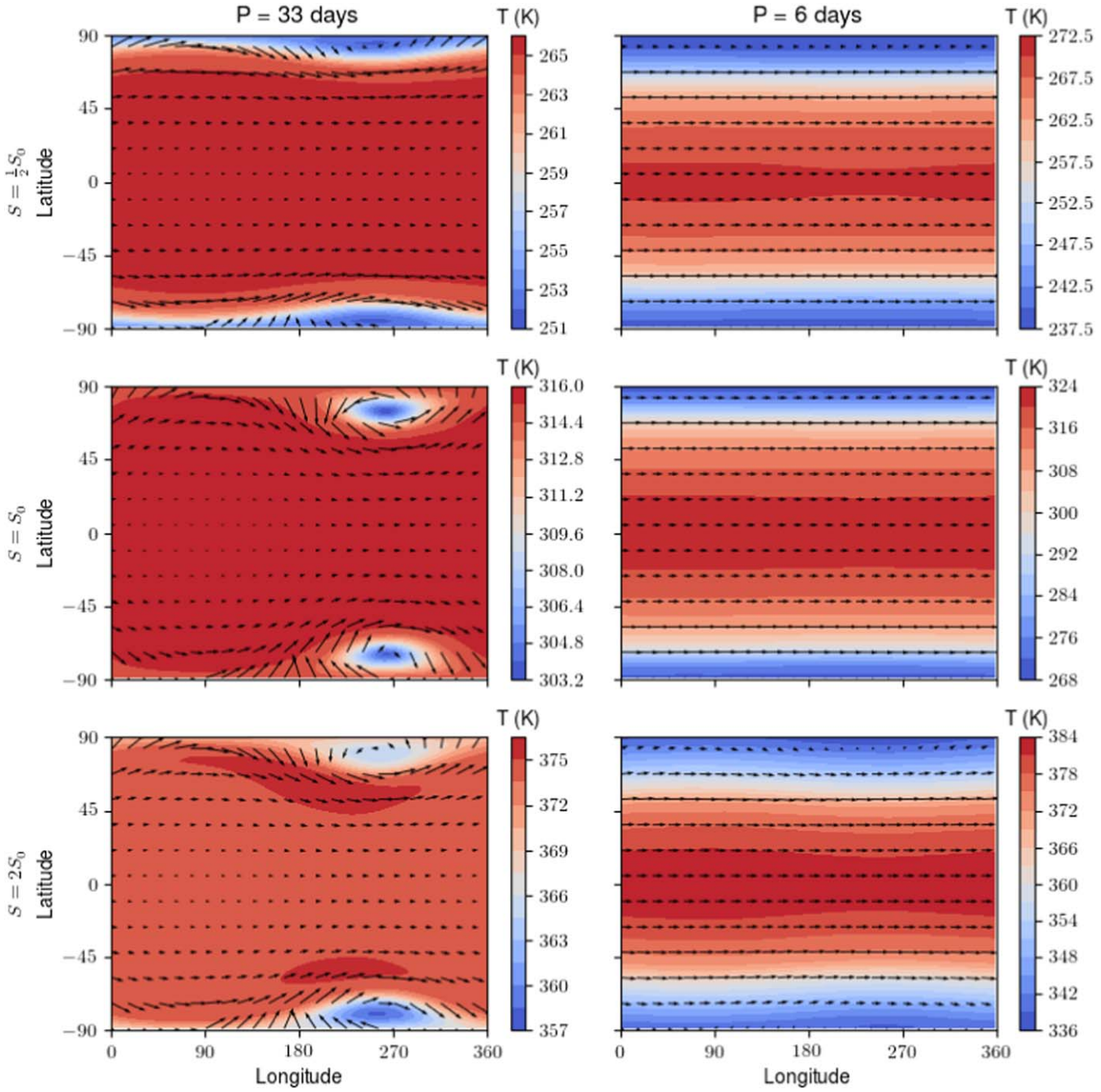


**Figure 3.** The 100 mbar level temperature profiles for the dry experiments. For the 33 day period experiments, the temperature varies on the order of 1 K throughout most of the horizontal plane apart from at a cold spot near (but offset from) the poles. For the 6 day period experiments, there is a much larger temperature drop from the equator to the pole. Note that the substellar point is at 0° longitude.

$$\mathrm{Ro}^2(\boldsymbol{u}\cdot\nabla u - uv\tan\phi) - \mathrm{Ro}\cdot fv = -\Lambda^2\partial_x\Phi, \tag{9}$$

where Ro is the Rossby number, $U/(\Lambda a)$, and $\Lambda$ is the weak temperature gradient (WTG) parameter $c_0/(\Lambda a)$ (Pierrehumbert & Ding 2016; Pierrehumbert & Hammond 2019), which is the ratio of the Rossby deformation radius to the planetary radius. $c_0$ is a characteristic wave speed. If we approximate the atmosphere as isothermal with characteristic temperature $T$, this wave speed $\sim\sqrt{RT}$. For weak horizontal temperature gradients, we require $\Lambda \gg 1$ and $\mathrm{Ro} \gg 1$ such that $\partial_x\Phi \sim \partial_x T \approx 0$. Using estimates from our experiments, the 33 day period simulations have $\mathrm{Ro} \approx 10$, $\Lambda \approx 30$, while the 6 day period simulations have $\mathrm{Ro} \approx 3$, $\Lambda \approx 10$, confirming that both cases are firmly within the WTG regime, with the slower-rotating experiments expected to be more strongly uniform in temperature. In contrast, temperate terrestrial simulations (such as Pierrehumbert & Hammond 2019) often have high-$\mu$ atmospheres, making $\Lambda < 1$ and exciting a strong wave response. GJ 1214b, being much hotter and faster rotating, has $\Lambda \approx 1$, being greater than or less than 1 depending on the assumed metallicity of its atmosphere (see Section 4.1).

This result can also be interpreted using the theory from Zhang & Showman (2017) in the low-drag limit, where the day–night temperature contrast compared to the equilibrium

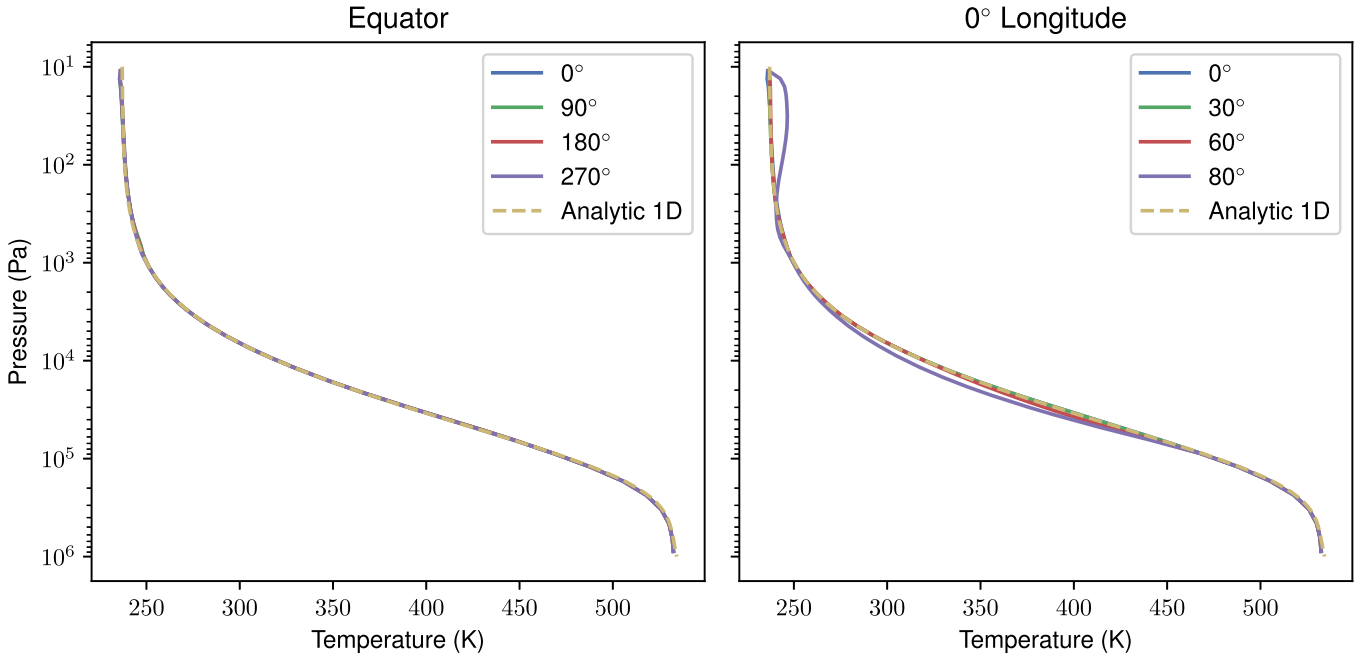


**Figure 4.** Vertical temperature profiles for the control experiment. Left: On the equator, the temperature profiles are very uniform and conform to the analytic 1D solution. Right: In the latitudinal direction, there are deviations from uniform temperature gradients, but only near the poles.

contrast is given by

$$\frac{\Delta T}{\Delta T_{\rm eq}} \sim 1 - \frac{2}{\alpha + \sqrt{\alpha^2 + 4\gamma^2}}, \tag{10a}$$

$$\alpha = 1 + \frac{\Omega \tau_{\rm w}^2}{\tau_{\rm r} \Delta \ln p}, \tag{10b}$$

$$\gamma = \frac{\tau_{\rm w}^2}{\tau_{\rm r} \tau_{\rm a,eq} \Delta \ln p}, \tag{10c}$$

where $\tau_{\rm r}$, $\tau_{\rm w}$, and $\tau_{\rm a,eq}$ are the radiative, wave, and cyclostrophic advective timescales, respectively (Zhang & Showman 2017). If we write the wave timescale as $a/\sqrt{RT} = 1/(\Omega\Lambda)$ and the advective timescale as

$$\tau_{\rm a,eq} = \frac{a}{U_{\rm eq}}, \tag{11}$$

$$= \frac{a}{\sqrt{R \Delta T_{\rm eq} \ln p}}, \tag{12}$$

$$= \frac{1}{\kappa \Lambda \Omega \sqrt{\ln p}}, \tag{13}$$

where $\kappa^2 \ll 1$ is the ratio between the equilibrium day–night temperature difference and the characteristic temperature of the atmosphere, then

$$\alpha = 1 + \frac{1}{\tau_{\rm r} \Omega \Lambda^2 \Delta \ln p}, \tag{14}$$

$$\gamma = \frac{\kappa \sqrt{\ln p}}{\Lambda \tau_{\rm r} \Omega}. \tag{15}$$

The radiative timescale at the $\tau = 1$ level can be estimated as

$$\tau_{\rm r} = \frac{c_p p(\tau = 1)}{4\sigma T^3 g} = \frac{c_p p_s}{4\sigma T^3 g \tau_{\rm LW}} \approx 8 \text{ days}, \tag{16}$$

which means $(\tau_{\rm r}\Omega)^{-1} = 1$ for the $P = 33$ days experiment and 0.1 for the $P = 6$ day experiments. Therefore, in all our experiments, we predict $\alpha \approx 1$ and $\gamma \ll 1$, which corresponds to $\Delta T/\Delta T_{\rm eq} \ll 1$.

### 3.3. Zonal Circulation

Next, we look at the zonal circulation. The temperature and wind profiles in our model runs were largely zonally symmetric, meaning the zonally averaged circulation is a good way of reducing the dimensions of the output data. Figure 5 shows the zonal-mean zonal wind of each experiment. The common feature of all the circulations is the presence of two high-latitude cyclostrophic jets that are in steady-state balance. Figure 6 shows the nonnegligible terms in the zonally averaged meridional momentum equation:

$$\frac{1}{a}[v\partial_\phi v] + \frac{[u^2]\tan\phi}{a} + [fu] = -\frac{1}{a}[\partial_\phi \Phi], \tag{17}$$

where $[\cdot]$ represents zonally averaged terms. The experiments with the shorter period orbit are very close to the gradient-wind balance, with the pressure gradient induced by the temperature contrast between the equatorial regions and the polar regions balanced by the Coriolis forces and cyclostrophic terms in the momentum equation. In contrast, in the slower-rotating experiments, nonlinear advective terms become important near the poles, where the meridional wind reaches its maximum magnitude value. Table 4 shows the maximum value of the time-averaged meridional velocity in each of the experiments, from which it is clear that the meridional velocity is an order of magnitude stronger in the slower-rotating experiment.

We do not currently have a theory for predicting the strength of this zonal circulation. The gradient-wind balance shown in Figure 6 is a diagnostic balance that does not illuminate how the atmosphere arrives in its final state. In other GCM studies of TL exoplanets (Komacek & Showman 2016; Zhang &

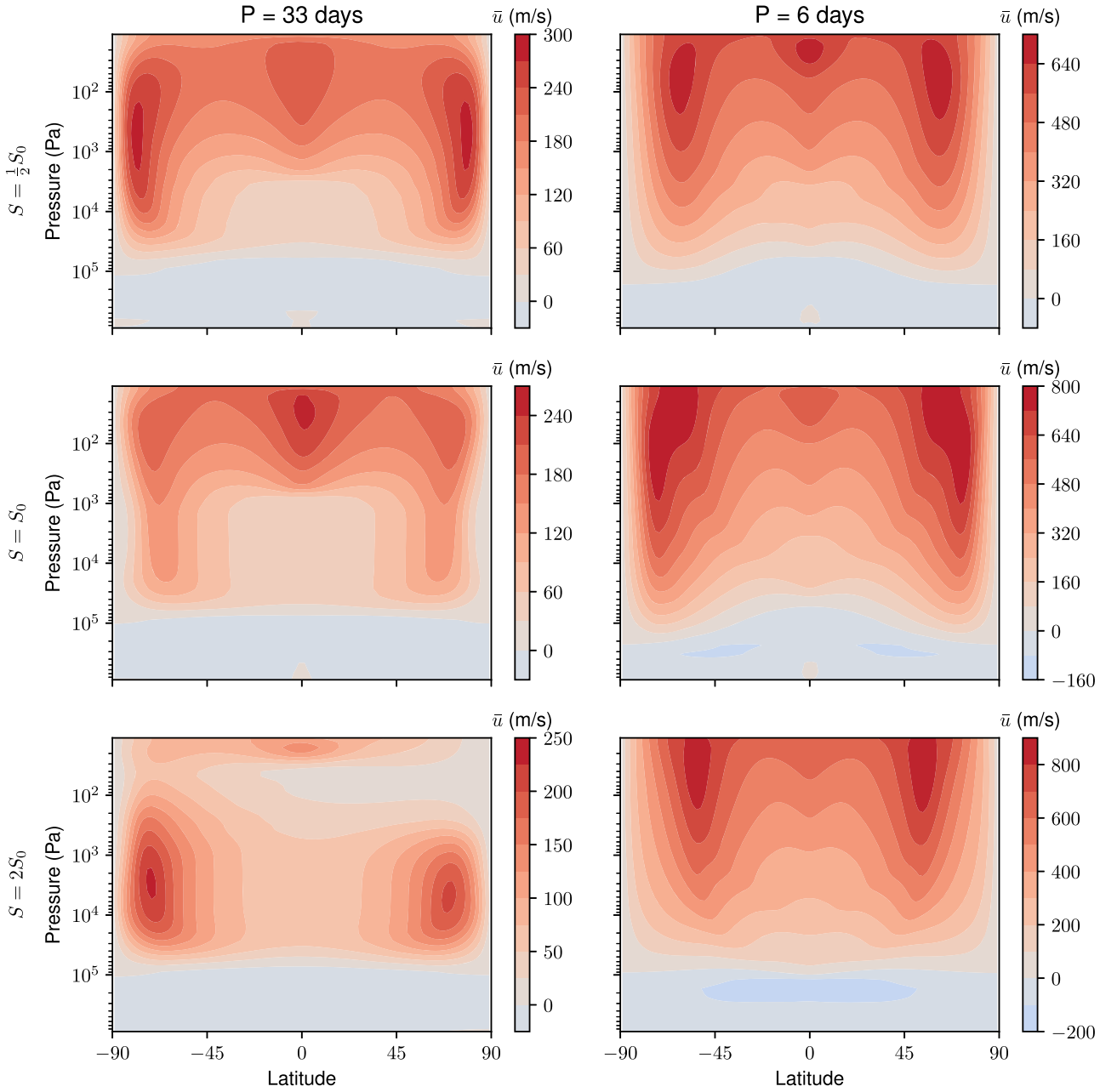


**Figure 5.** The zonal-mean zonal wind for each of the experiments. All circulations exhibit high-latitude cyclostrophic jets. All experiments show equatorial superrotation, in some cases forming a third maximum on the equator.

Showman 2017), the rms wind is linked to the advective, wave, and radiative timescales. However, in these studies, the wind speed also depends on an equilibrium temperature profile which is prescribed in the model. In our gray-gas model, this equilibrium temperature profile is not known a priori, which makes it difficult to produce similar scaling relations. We note that at each rotation rate, the zonal jet strength is approximately the same at each instellation, but that it increases greatly with increasing rotation rate. An angular momentum conserving wind moving from the equator with $u = 0$ would have speed

$$u_{\mathrm{AM}} = a\Omega\frac{\sin^2\phi}{\cos\phi} \tag{18}$$

at latitude $\phi$. For jets at $\phi = 75°$, this gives $u_{\mathrm{AM}} = 130\ \mathrm{m\ s^{-1}}$ for the 33 day period case and $u_{\mathrm{AM}} = 730\ \mathrm{m\ s^{-1}}$ for the 6 day period case, which is of the correct order of magnitude as the results in Figure 5. However, we note that there is no requirement for the zonal wind speed to be 0 at the equator (as in a classical Hadley circulation) because there is no friction at the bottom of the model. We investigate the overturning circulation in the next section.

### 3.4. Overturning Circulation

To investigate the origin of the high-latitude zonal jets, we look at the mean meridional overturning circulation. In the conventional $(\lambda, \phi)$ coordinate system, the mass stream function is given by

$$\psi_m(\phi, p) = \frac{2\pi a\cos\phi}{g}\int_0^p [v](\phi, p')dp', \tag{19}$$

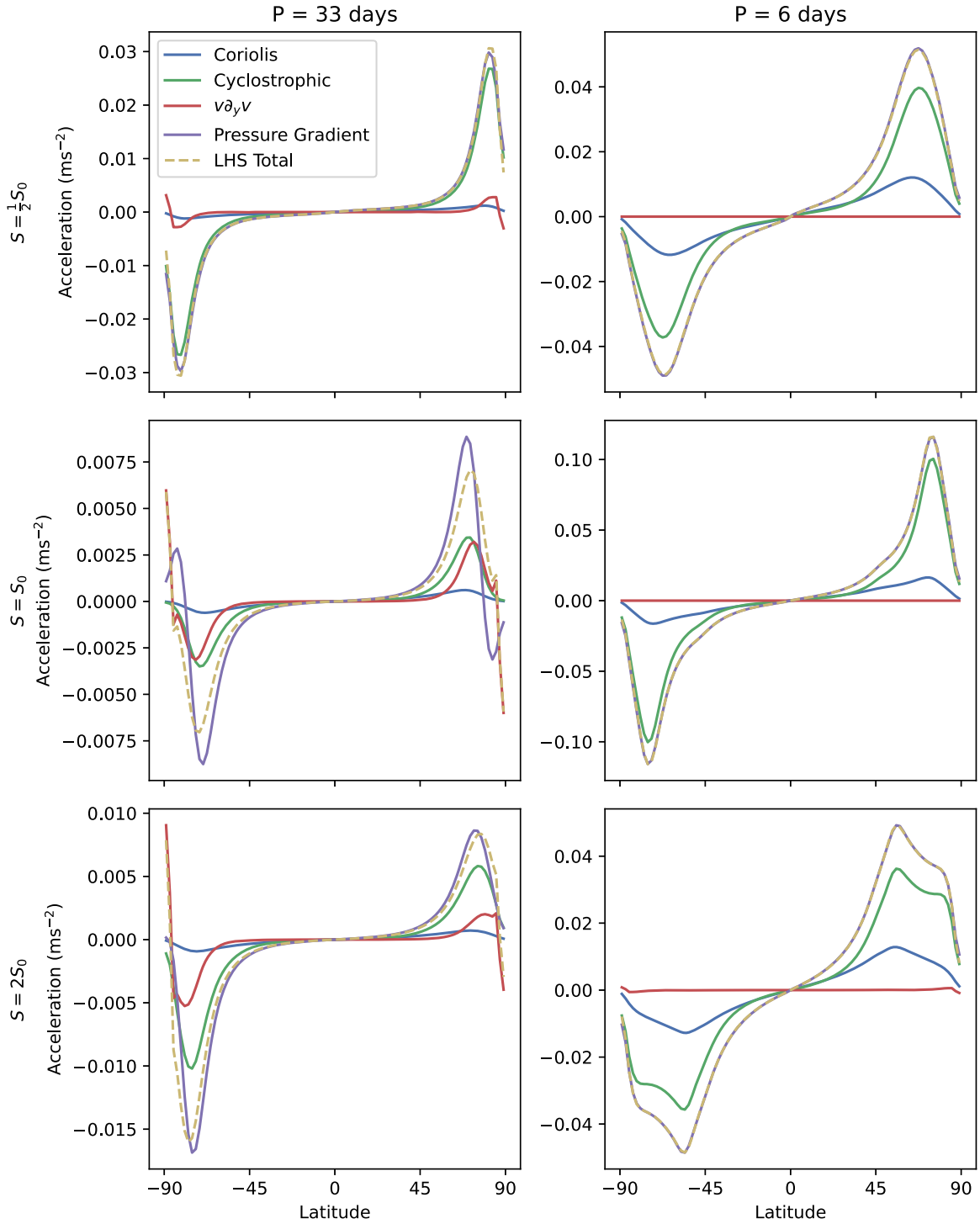


**Figure 6.** Meridional momentum balance for each of the dry simulations at the 10 mbar level. For the 6 day period experiments (right-hand side), classical gradient-wind balance sustains the jets, whereas in the 33 day period experiments the nonlinear advection term is also significant to the balance.

**Table 4**
Maximum Meridional Velocity in the Time-averaged Flow

| Experiment name | Maximum $v$ (m s$^{-1}$) |
|---|---|
| PKh | 193 |
| PKc | 265 |
| PKd | 383 |
| P6h | 7 |
| P6c | 13 |
| P6d | 29 |

which represents the meridional mass flux between the top of the atmosphere ($p = 0$) and a pressure level $p$. Figure 7 shows this mass stream function for all the experiments. The zonal-mean circulation follows contours of constant $\psi_m$, so positive (red) regions indicate clockwise circulation around contours and negative (blue) regions counterclockwise circulation. In all six cases we see a net overturning circulation from the equator to pole in both hemispheres. In the 33 day period experiments, we also see two separate cells appear in each hemisphere, with

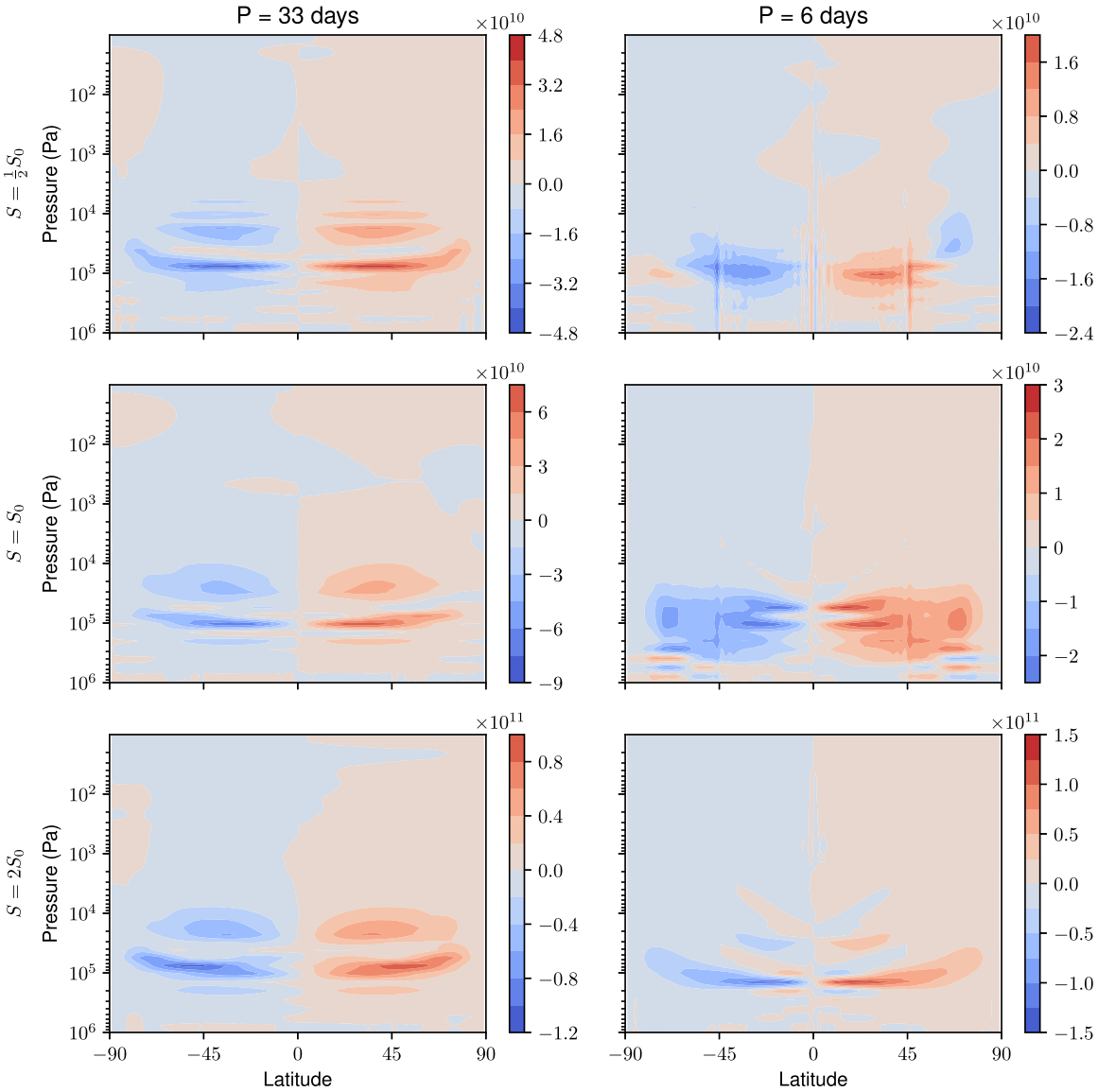


**Figure 7.** The meridional mass stream function (contours in units of kg $s^{-1}$). All the experiments show some form of net overturning from the equator to the pole.

one centered at approximately $2 \times 10^4$ Pa and another centered at around $1 \times 10^5$ Pa. In the theory of nonsynchronously rotating planets, having Ro $\gg 1$ leads to a global Hadley-like circulation (e.g., Venus and Titan), which transports energy from the tropics to the poles to balance the gradient in stellar heating (Held & Hou 1980; Kaspi & Showman 2015; Vallis 2017). This Hadley circulation also transports angular from the equator polewards and spins up subtropical jets on Earth. Our experiments differ from the classical Held–Hou model in two main ways: first, we do not have a drag layer at the bottom of the atmosphere that can inject angular momentum into the atmospheric flow by imposing a torque on the westward-moving surface flow. Our experiments conserve the integrated angular momentum of the atmosphere to 1 part in 1000 over the total simulation time (with losses due to numerical dissipation). Second, the forcing in our model is nonaxisymmetric and is centered on the substellar point, meaning the main heating contrast is between substellar and antistellar points in contrast to between equator and pole, as in the canonical analysis.

Because there is no surface to inject angular momentum into our atmosphere, the positive angular momentum associated with jets in the upper atmosphere is balanced by a retrograde circulation in the lower atmosphere. Spinning up from rest, the radiative heating at the equator causes rising motion there. Air moving poleward higher up in the atmosphere rotates in the prograde direction, conserving angular momentum, whereas the return flow will have retrograde motion in the absence of friction. How these two circulations interact is unclear and requires more study. As mentioned above, because $u$ is not fixed at 0 at the equator, it is difficult to use this as a theory to predict the jet speed away from the equator. However, the qualitative picture of air from the equator moving poleward and accelerating the jets provides a rough order-of-magnitude estimate of the jet wind speeds.

Figure 8 shows the mass stream function of the control experiment during spin-up (averaged between 4000 and 5000 days). The overturning circulation that would spin up angular

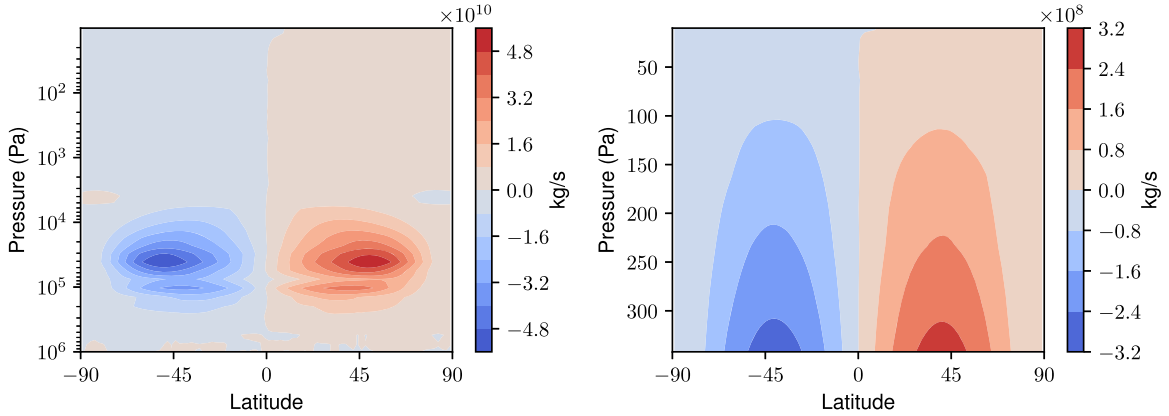


**Figure 8.** The mass stream function of the control experiment averaged between 4000 and 5000 days during spin-up. Left: a view of the whole atmosphere with its clear overturning circulation from equator to pole. Right: the upper atmosphere's stream function has a similar structure (though is obscured on the left due to the magnitude), highlighting that the upper atmosphere is spun up via a similar mechanism.

momentum conserving jets is clear on the left-hand panel. The picture in the upper atmosphere is similar (but the overturning circulation is weaker due to the lower mass of the upper atmosphere)

In previous studies of TL planets, the zonal circulation has sometimes been split into a day-side Hadley circulation and a night-side anti-Hadley circulation (e.g., Charnay et al. 2015a) —however, this can obscure a more direct circulation between day side and night side (Hammond & Lewis 2021). We therefore follow Hammond & Lewis (2021) in calculating the mass stream function in TL coordinates (Koll & Abbot 2015). The TL latitude, $\phi_{\rm TL}$, is 0° at the north and south poles, 90° at the substellar point and −90° at the antistellar point. The TL longitude, $\lambda_{\rm TL}$, is 0 on the semicircle passing through the substellar point, north pole, and antistellar point and increases toward the eastern terminator. To avoid ambiguity, we will use the term "the poles" to refer exclusively to the poles in the conventional latitude–longitude coordinate system and use "substellar point" and "antistellar point" to refer to the points at $\phi_{\rm TL} = 90°$ and $\phi_{\rm TL} = -90°$, respectively. In TL coordinates, one can define a stream function:

$$\psi_{\rm TL} = \frac{2\pi a \cos\phi_{\rm TL}}{g} \int_0^p [v_{\rm TL}]_{\rm TL}(\phi_{\rm TL}, p')dp, \tag{20}$$

where $[\cdot]_{\rm TL}$ represents an average over $\lambda_{\rm TL}$, and $v_{\rm TL}$ is the component of the wind in the direction of increasing $\phi_{\rm TL}$ (and not just the conventional meridional wind in a different coordinate system). Figure 9 shows the stream function in this coordinate system. In all experiments there is a direct day −night circulation driven by radiative heating. In the 6 day period experiments, there is also a small area of counter-circulation near the terminator. This is because the jet regions near the poles are associated with a downwelling region on the day side and upwelling on the night side. One can also see, in all six cases, that the flow is partially split into two subcirculations, with a stronger one on the day side and a weaker one on the night side. Thinking in terms of the conventional mass stream function, this would explain why we see a circulation from the equator to the pole—because the "anti-Hadley" circulation on the night side is weaker than the conventional Hadley-like circulation on the day side (due to weaker radiative forcing on the night side). This asymmetry between the day-side and night-side flow allows for a net transport of angular momentum from the equator to the pole, which accelerates the zonal jets.

We note that this circulation is on average an order of magnitude larger than the overturning circulation in latitude −longitude coordinates, confirming that this is the dominant overturning circulation.

To better distinguish the overturning circulation from the zonal jet structure, we decompose the horizontal winds into their divergent and rotational components (Hammond & Lewis 2021):

$$\boldsymbol{u} = \boldsymbol{u}_{\rm div} + \boldsymbol{u}_{\rm rot}, \tag{21a}$$

$$\boldsymbol{u}_{\rm rot} = \boldsymbol{k} \times \nabla\Psi, \tag{21b}$$

$$\boldsymbol{u}_{\rm div} = -\nabla\chi, \tag{21c}$$

where $\Psi$ is a stream function (distinct from the mass stream functions discussed) and $\chi$ is a velocity potential that can be calculated from the vorticity and divergence of the velocity respectively. Importantly, the meridional rotational velocity is given by $v_{\rm rot} = \partial_x\Psi$, which vanishes when averaged in the longitudinal direction. Therefore, the mass stream function depends only on the divergent component of the velocity field. This is true in both conventional latitude−longitude and TL coordinate systems.

Figure 10 shows the total, rotational, and divergent winds for the control experiment at 100 mbar, along with the pressure velocity. We find that the velocity is dominated by the rotational component with magnitude on the order of 100 m s$^{-1}$. However, the divergent component responsible for the overturning circulation, shown in the bottom of Figure 10, is predominantly directed from day side to night side (with some erratic behavior at the conventional north and south poles, most likely due to regridding errors).

We estimate the dependence of the magnitude of the TL stream function on instellation using the steady-state equation for the transport of dry static energy, $s \equiv c_p T + \Phi$:

$$\nabla\,(s\boldsymbol{u}_{\rm TL}) = \dot{Q}, \tag{22}$$

where $\dot{Q}$ is the heating rate per unit mass. Taking the average over the TL longitude and integrating over $dp/g$, we find

$$\int_0^p \frac{dp}{g} \frac{1}{a\cos\phi} \partial_\phi [v_{\rm TL} s \cos\phi] = [S - F], \tag{23}$$

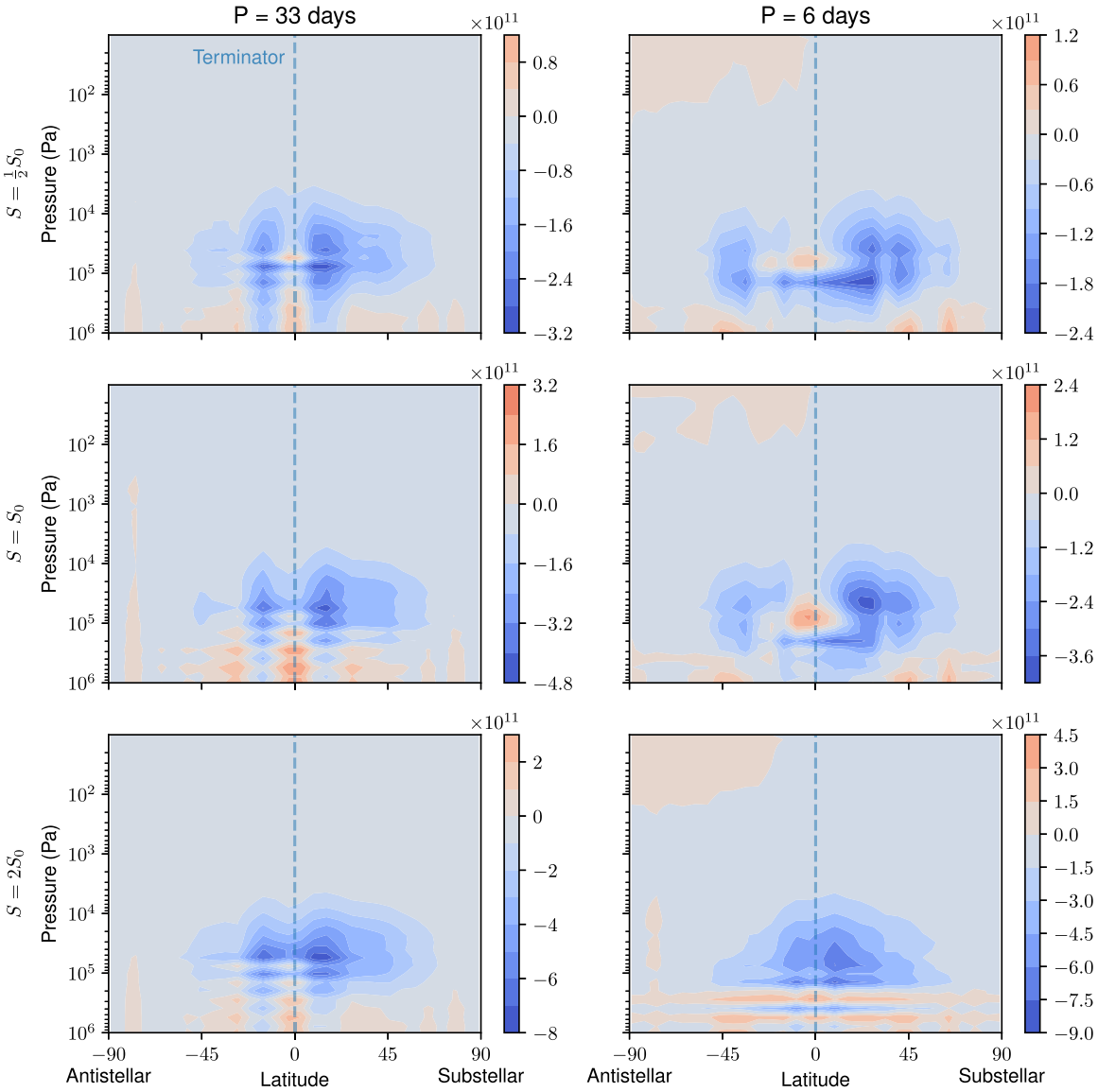


**Figure 9.** The tidally locked mass stream function, $\psi_{\rm TL}$ (units kg s$^{-1}$). This shows more clearly the stronger overturning circulation between the day side and night side (see Figure 7).

where $S$ is the pressure-integrated solar heating and $F$ is the pressure-integrated outgoing flux. We have also used the fact that $\omega s = 0$ at both $p = 0$ (true from the boundary condition $\omega = 0$ there), and at the level and latitude of the maximum of the TL stream function (also true because $\omega \sim \partial\psi/\partial\phi = 0$, where $\psi_{\rm TL}$ is maximal). We now approximate this equation to find a scaling balance of terms by making a series of approximations. First, we assume that the dry static energy and $v_{\rm TL}$ are uncorrelated in the zonal and vertical directions. We also assume that if the temperature gradients are weak enough, then $\Delta s/s \ll \Delta v/v$ such that

$$\int_0^p \frac{dp}{g}\frac{1}{a\cos\phi}\partial_\phi[v_{\rm TL} s\cos_\phi], \tag{24}$$

$$\approx \langle [s]\rangle \int_0^p \frac{dp}{g}\frac{1}{a\cos\phi}\partial_\phi([v_{\rm TL}]\cos\phi), \tag{25}$$

where $\langle\cdot\rangle$ represents a column average. Note that the integral term in Equation (25) is proportional to $\omega$, which is, in turn, proportional to $\partial_\phi\psi_{\rm TL}$. To approximate $[S-F]$, we note that when $p \to p_s$, $S$ becomes the incoming stellar radiation and $F$ the OLR, which vary over the scale $S_0$ in the $\phi_{\rm TL}$ direction. We approximate that this scaling holds at the level of the maximum stream function too. Thus, we get the scaling:

$$\psi_{\rm TL} \sim \frac{a^2 S_0}{\langle [s]\rangle}. \tag{26}$$

The dry static energy, $s = c_p T + \Phi$, scales as $\max(c_p T, \Phi) \sim T \sim S_0^{1/4}$ if we assume $\Phi \approx RT$ i.e., the region integrated over is roughly one scale height. This gives the final scaling $\psi_{\rm TL} \sim S_0^{3/4}$. Note that there is no dependence on the rotation rate in this expression.

Figure 11(a) shows the maximum absolute value of the TL stream function from five experiments at different instellations. The best-fit power-law relation has exponent $0.72 \pm 0.04$, which is in agreement with the theoretical prediction of $\frac{3}{4}$.

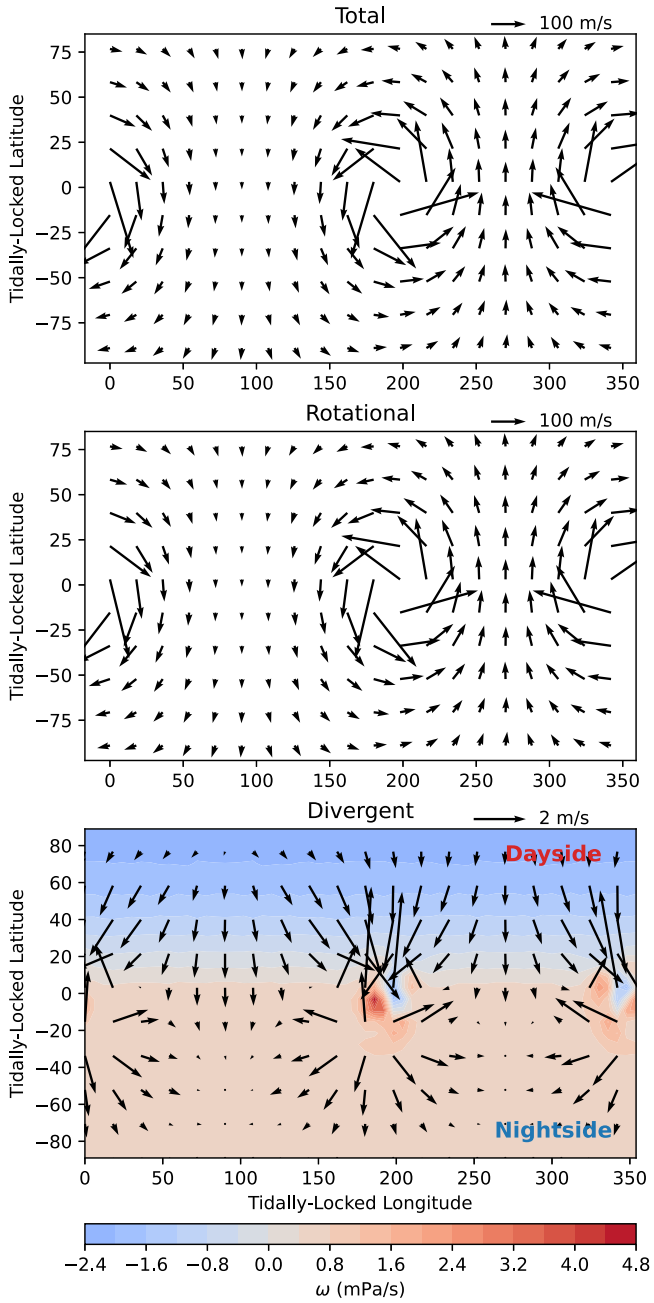


**Figure 10.** Total, rotational, and divergent components of the wind field of the control experiment at 100 mbar. The rotational component of the wind dominates the circulation, but the small divergent component is responsible for the mass transport between the day side and night side. The bottom plot also shows the pressure velocity, $\omega$, which illustrates the upwelling on the day side and downwelling on the night side of the planet.

We can also use this theory to predict the characteristic vertical velocity of the overturning circulation. The vertical velocity, $w = dz/dt$, is related to the pressure velocity $\omega$ by

$$w = -\frac{1}{\rho g}\omega = -\frac{RT}{pg}\omega. \tag{27}$$

The pressure velocity is linked to the stream function by

$$\omega = -\frac{g}{2\pi a^2 \cos\phi}\frac{\partial \psi_{\mathrm{TL}}}{\partial \phi}. \tag{28}$$

Combining these two equations and using $\partial_\phi \psi_{\mathrm{TL}} \sim \psi_{\mathrm{TL}} \sim a^2 S/\langle [s] \rangle$, we get

$$w \sim \frac{S_0}{p}. \tag{29}$$

Note this scaling assumes that the pressure level of maximum vertical velocity is the same as the pressure level of the maximum stream function. In all our experiments, although $S_0$ is varied, the gray opacities stay the same, so the level of maximum radiative heating (linked to the level of maximum upwelling by the WTG approximation) stays approximately the same. We find that the maximum value of $w$ in all experiments is at $p \approx 2 \times 10^4$ Pa, in which case $w \sim S_0$. Figure 11 confirms this dependence, with the best-fit line having an exponent of $1.02 \pm 0.02$, in agreement with theory.

### 3.5. Equatorial Superrotation

In each of the experiments shown in Figure 5, there is equatorial superrotation. There are two main types of mechanisms thought to drive superrotation in planetary atmospheres (Wang & Mitchell 2014). The first is through generating eddies from nonaxisymmetric forcing, e.g., via TL solar heating (Showman & Polvani 2011; Tsai et al. 2014; Hammond & Pierrehumbert 2018) or from convective heating (e.g., Lian & Showman 2010; Liu & Schneider 2011). The second is from shear instabilities in atmospheres with axisymmetric forcing (e.g., Iga & Matsuda 2005), which is observed in idealized simulations of slow-rotating planets (Mitchell & Vallis 2010) and proposed as a potential mechanism driving superrotation in Titan's atmosphere (Wang & Mitchell 2014).

In our simulations, there are two distinct types of superrotation. During spin-up, we get superrotation at the equator at the pressure levels of radiative heating, which is likely due to the stationary-wave response to the radiative forcing. Because we are strongly in the weak temperature gradient regime (with a low-mean-molecular-weight atmosphere and slow rotation rate), the Rossby radius of deformation is large, and there is only a weak excitation of equatorial Rossby and Kelvin waves required to drive superrotating jets, which are often seen in simulations of TL terrestrial exoplanets (e.g., Pierrehumbert & Hammond 2019). This is most likely the reason we do not see an on-equator maximum of zonal wind in the lower atmosphere (at around $10^4$–$10^5$ Pa).

In the upper atmosphere, however, we see a sudden transition to superrotation caused by an instability. Figure 12 shows the development of superrotation in the upper atmosphere over a period of ≈40 days, where momentum is transported from the high-latitude jet toward the equator.

We performed additional experiments to test whether the location of the upper boundary or the damping in the sponge layers affected the presence of the instability. The model top of a GCM provides a challenge because often nonphysical boundary conditions have to be specified to ease solving the governing equations numerically. In ExoFMS, there is an $\omega = 0$ boundary condition that keeps the model top fixed at a constant pressure. This can lead to the spurious reflection of waves from the model top, which are removed by introducing some form of damping to the top model layers (known as a sponge layer). Our model gradually increases the divergence damping coefficient toward

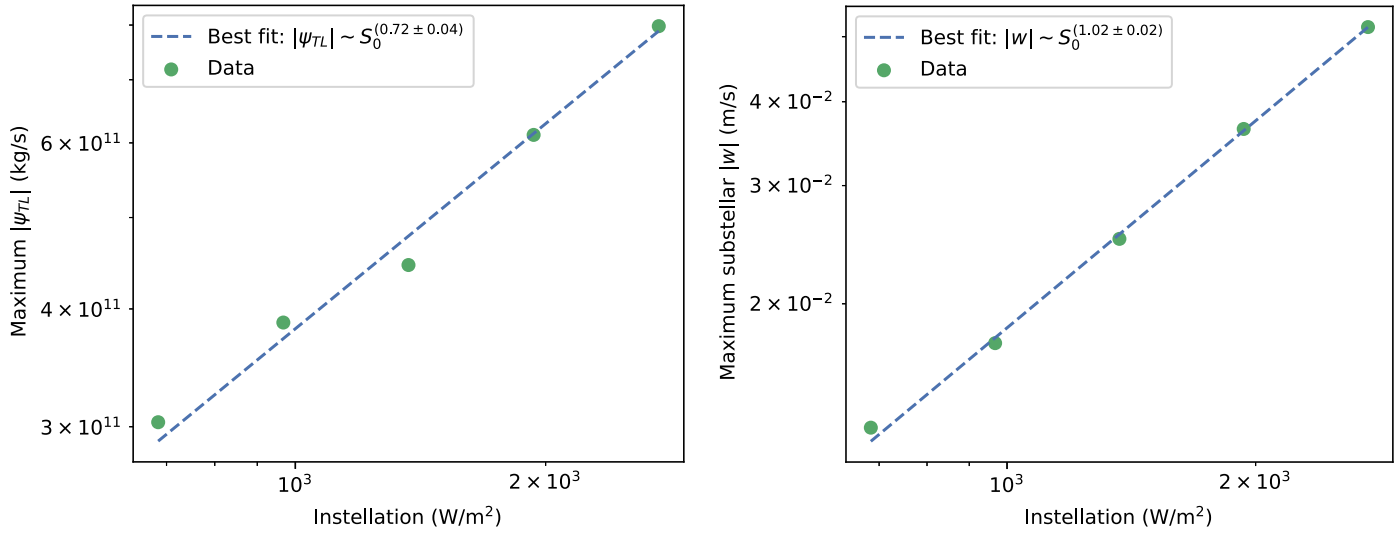


**Figure 11.** (a) The maximum absolute value of the tidally locked stream function as a function of instellation. The best-fit power law to the data shows $\psi_{\rm TL} \sim S_0^{0.72 \pm 0.04}$, which is in agreement with the theoretical exponent, 0.75. (b) The maximum value of the vertical velocity, $w$, at the substellar point as a function of instellation. The best-fit power law to the data shows $w \sim S_0^{1.02 \pm 0.02}$, which is in agreement with the theoretical exponent, 1.

the model top as

$$d_2 = d_{2,0}\left[1\text{–}3\tanh\left(\frac{1}{10}\log\left(\frac{p}{p_0}\right)\right)\right], \tag{30}$$

where $d_{2,0}$ is a constant coefficient, set to 0.02 in our simulations —large enough to maintain model stability but small enough not to affect the angular momentum budget of the atmosphere (Lee et al. 2021). In the top two layers, the value of $d_{2,0}$ is doubled then quadrupled respectively to provide a stronger sponge-layer damping.

To test the robustness of the superrotation, first we reduced the model-top pressure by a factor of 100, from 10 to 0.1 Pa. We found that the instability still occurred, but at a lower pressure of around 2 Pa (see 40 Pa in the 10 Pa model top simulations). In the 33 day period experiments, we noted that the onset of superrotation occurred at a much later time, usually around 10,000–13,000 days, around the time when the high-latitude zonal jets have extended to the top of the atmosphere. This, along with our experiment changing the model top pressure, suggests that model-top effects could be playing a role in triggering the instability.

Second, we changed removed the pressure dependence of $d_{2,0}$ and set it to its minimal value. This had little effect on the outcome of the simulations, with the instability occurring at a similar pressure level and time as the control. This proves that the instability is not an artifact of the increase in divergence damping near the sponge layer.

Lastly, we increased the depth and strength of the sponge layer, such that the top five layers were sponge layers, and increased the damping divergence coefficient to 0.05. In this experiment, the instability still occurred, but the magnitude of the resulting equatorial zonal wind was reduced by around a factor of 2.

Note that divergence damping is only one choice of sponge-layer mechanism. Another common choice is the presence of Rayleigh friction in the top layers. However, we did not use this because it is known to actively violate angular momentum conservation and have implications for the upper atmosphere (Shaw & Shepherd 2007; Jablonowski & Williamson 2011, pp. 381–493). We proceed with our analysis, noting that this feature of the circulation seems to be robust to changes in damping but not ruling out that the model top could affect the circulation.

If we look at the zonal-eddy height field, $h^*$ as a function of time at the 40 Pa level (Figure 13), we see that there is an eastward-traveling disturbance that couples the equatorial region to the vortices near the pole. We note that the pattern of disturbance looks similar to the eddy height fields seen in Mitchell & Vallis (2010) (Figure 14) and the pressure perturbation fields in Wang & Mitchell (2014) (Figures 1 and 2), suggesting that a Rossby–Kelvin (RK) instability may be responsible for the acceleration of the superrotation. The RK instability is caused by a coupling of equatorial Kelvin waves and high-latitude Rossby waves and occurs in the regime where the Froude number of the flow (the ratio between the frequency of the Rossby and Kelvin waves) is between 1–3 (Wang & Mitchell 2014). The Froude number is given by

$$\mathrm{Fr} = \frac{U_0/\cos(\phi_{\max})}{U_{\rm eq} + NH/m}, \tag{31}$$

where $U_0$ is the high-latitude jet speed at latitude $\phi_{\max}$, $U_{\rm eq}$ is the equatorial wind speed, $N$ is the buoyancy frequency, $H$ the scale height of the disturbance, and $m$ the vertical wavenumber (i.e., $m = 1$ represents the gravest baroclinic mode of disturbance). Because the disturbance occurs in the upper atmosphere of our model where the gray-gas equilibrium temperature is constant, we can approximate $NH \approx \sqrt{RT_s}$, where $T_s$ is the skin temperature of the atmosphere. Ignoring the equatorial wind speed during instability, we approximate Fr using $U_0 \approx 400\,\mathrm{ms}^{-1}$, $\phi_{\max} \approx 75°$, and $T_s \approx 230$ K, which give a Froude number of ≈1.6, placing the

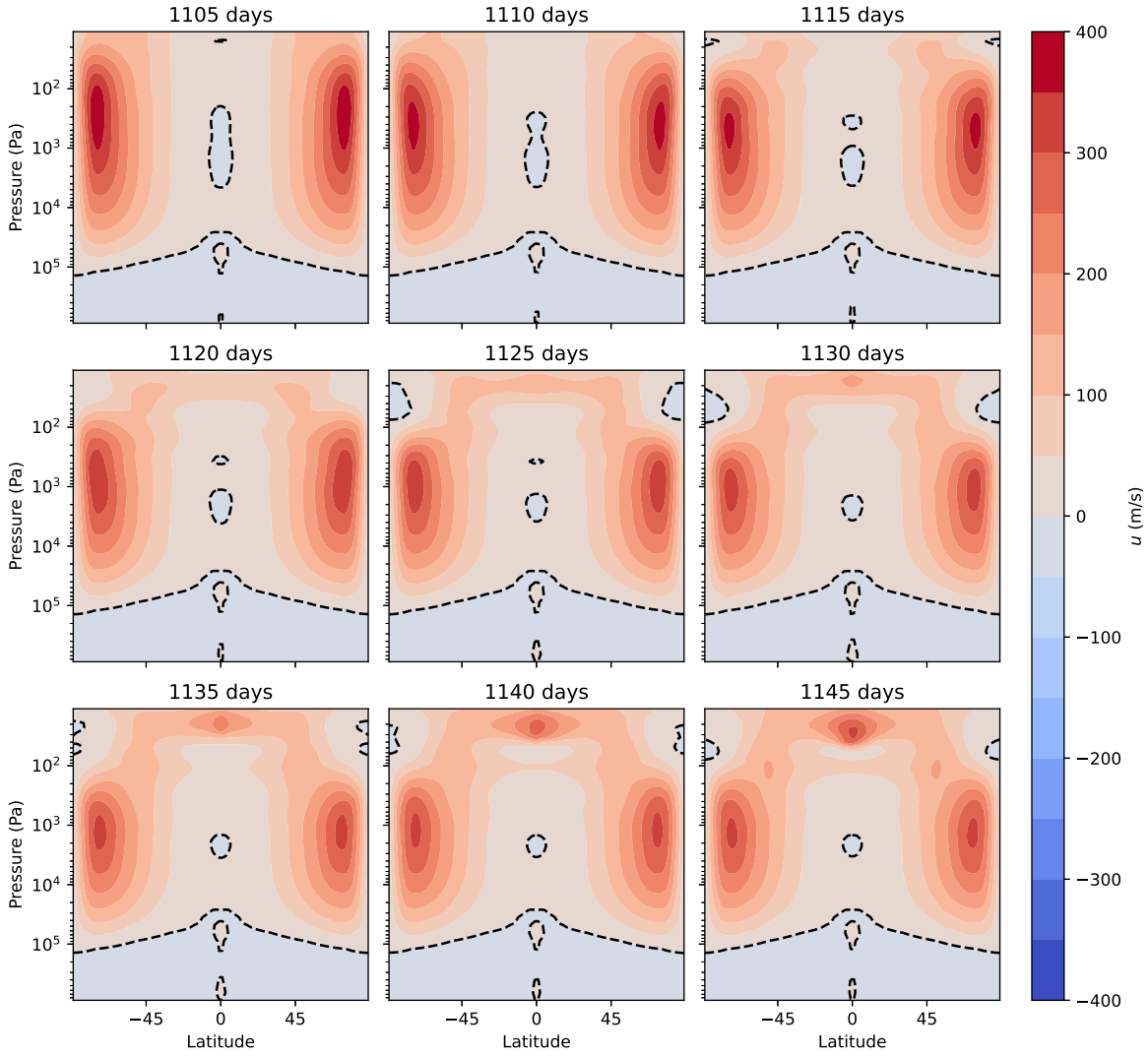


**Figure 12.** The zonal-mean zonal wind of the P6h run during the development of the transient instability causing superrotation. On the timescale of tens of days, momentum in the upper atmosphere is transferred from the poles to the equator. The $u = 0$ contour is marked by the dashed black line.

atmosphere in the correct parameter regime for the RK instability to take place.

Figure 14 shows the Hovmöller diagram of the zonal-eddy height field. There is a clear eastward-traveling wave pattern in the horizontal equatorial structure with constant phase velocity. In the high-latitude regions, this structure remains but with an added beating in the pattern. Performing a Fourier transform in both time and space, we extract the phase speed of the eastward-traveling component and find it to be around $330\,\mathrm{ms}^{-1}$ at the equator, comparable to the speed of the high-latitude jets and to a characteristic Kelvin-wave timescale, which is on the order of hundreds of m $s^{-1}$. Performing this Fourier transform on the high-latitude data also confirms that the beating pattern in the high-latitude data is at 0 frequency, and represents the zonal wavenumber 1 time-mean background in the height field. The vertical structure of the wave pattern is more complicated but somewhat resembles a standing-wave structure near the equator, suggesting the instability could be equivalent-barotropic in nature.

Lastly, we show that this wave structure directly leads to the acceleration of zonal wind at the momentum. If we decompose the zonal-mean zonal wind equation into mean, zonal-eddy, and time-eddy components, we get

$$\frac{\partial[\bar{u}]}{\partial t} = -\frac{1}{a\cos^2\phi}\partial_\phi\{([\bar{u}][\bar{v}] + \underbrace{[\bar{u}^*\bar{v}^*]}_{\substack{\text{stationary}\\ \text{eddies}}} + \underbrace{[\overline{u'v'}]}_{\substack{\text{transient}\\ \text{eddies}}})\cos^2\phi\}$$
$$\underbrace{\phantom{[\bar{u}][\bar{v}]}}_{\substack{\text{mean}\\ \text{flow}}}$$
$$+\omega \text{ terms, Coriolis terms, etc.,} \tag{32}$$

where overlined and bracketed terms represent time and zonal means, respectively, and starred and dashed terms represent deviations from time and zonal means, respectively. This equation represents the meridional flux of momentum due to the mean flow, stationary eddies, and transient eddies on the mean jet speed. Figure 15 shows the three horizontal terms in Equation (32) as a function of latitude. The mean flow acts to transport momentum away from the equator (positive gradient), whereas both the stationary and transient eddies pump momentum toward the equator, with the eddy accelerations dominating, helping to accelerate the equatorial jet at this level.

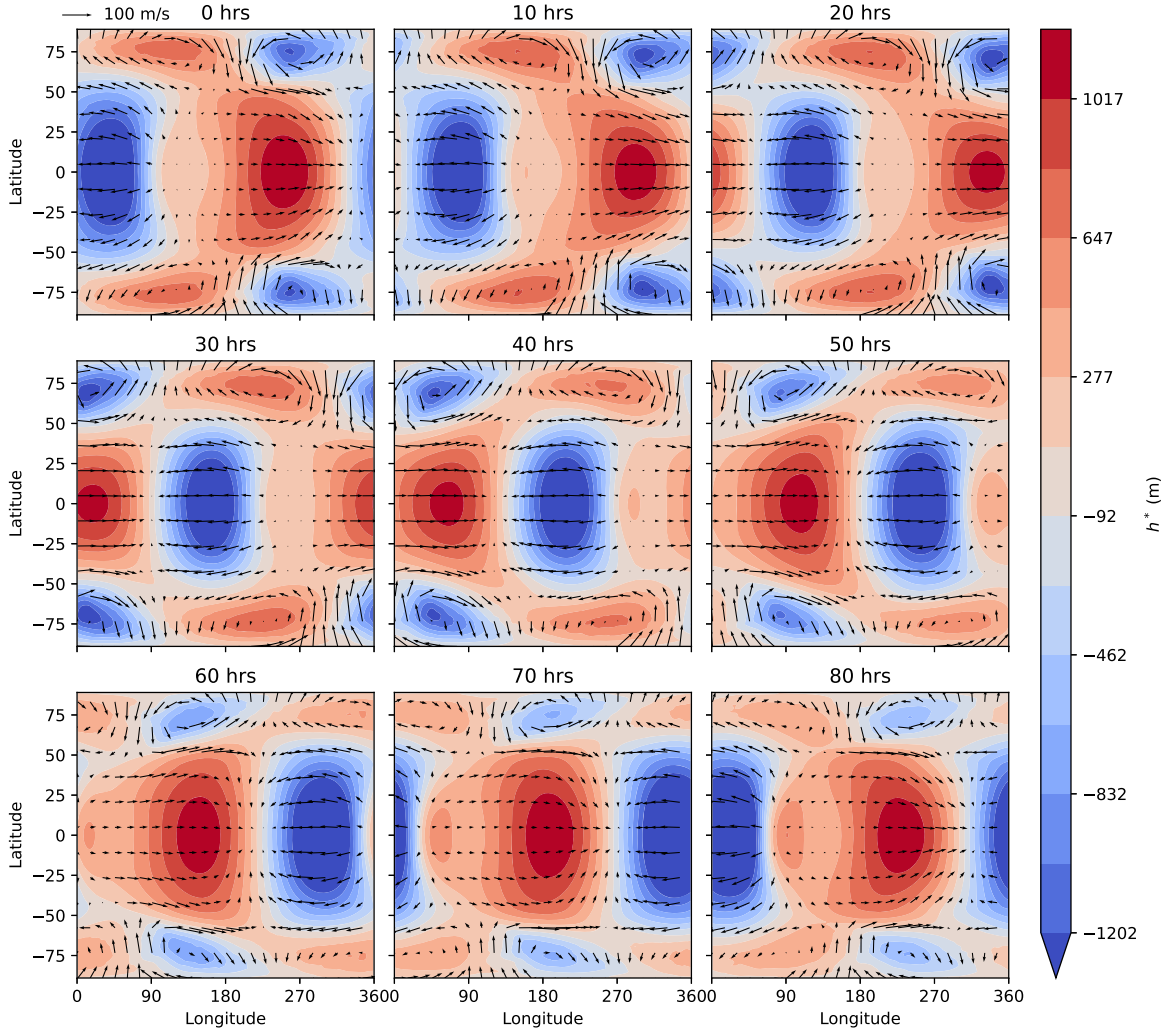


**Figure 13.** The zonal-eddy height field, $h^*$, across an 80 hr period of time during which the instability is forming. The arrows represent the zonal-eddy wind field. There is an eastward-traveling wave-like disturbance with zonal wavenumber 1.

## 4. Discussion

### 4.1. Comparison to Other Studies

On a qualitative level, our results look most similar to previous studies of sub-Neptune GJ 1214b with solar metallicity, such as those found in Kataria et al. (2014) and Drummond et al. (2018), who find high-latitude jets and also superrotation near the top of the atmosphere. Our results also look qualitatively similar to those in Wang & Wordsworth (2020) at earlier model times (around 1000–2000 days), where they find two distinct high-latitude jets. However, in Wang & Wordsworth (2020) the jets collapse into one wide equatorial jet as the kinetic energy converges to equilibrium, which is not seen in our model. We note that although GJ 1214b is similar in radius to K2-18b, it has a rotation period of 1.58 days (Berta et al. 2011) so we would expect much more pronounced equatorial dynamics and a stronger stationary-wave acceleration of the equatorial jet. The greater instellation (23,600 $\mathrm{Wm}^{-2}$; Wang & Wordsworth 2020) has a much smaller effect on the WTG parameter (which goes as $T^{1/2} \sim S_0^{1/8}$) but will affect the dynamics via the radiative timescale, which will be much shorter and therefore with pronounced day–night temperature contrasts (Zhang & Showman 2017). Estimating the WTG parameter, $\Lambda = c_0/(\Omega a) \approx \sqrt{RT}/(\Omega a)$ (the last assumption being valid if we assume the dynamics occurs on a height scale greater than the atmospheric scale height) for GJ 1214 b using values found in Wang & Wordsworth (2020), we find $\Lambda = 1.8$ for solar metallicity. Thus, under the assumption of a low-mean-molecular-weight atmosphere, we might expect to see some qualitative features of the WTG regime in this atmosphere.

In studies of TL terrestrial planets, the regime in which the global Rossby radius exceeds planetary radius (i.e., the "slow-rotator" regime in Haqq-Misra et al. 2018 and "Type I" circulation in Noda et al. 2017) is associated with the predominant circulation being directly from day side to night side and isotropic around the substellar point. This contrasts with our finding of strong high-latitude jets and a residual equator-to-pole overturning circulation. However, we note that our model is optically thick to SW radiation, whereas terrestrial planet atmospheres are often optically thin to SW radiation and have a significant proportion of incoming stellar radiation absorbed at the surface. This drives convection and convectional heating of the troposphere, which may explain some disparities between models. Second, the surface is often parameterized with some form of drag at the bottom boundary, which is not present in our model. Lastly, terrestrial planets are typically modeled with an $N_2$-dominated atmosphere. Increasing the molecular weight of the atmosphere decreases $\Lambda$ (because $R \propto \mu^{-1}$) and also decreases the heat capacity (which is proportional to $R$ in the case of an ideal gas with a constant

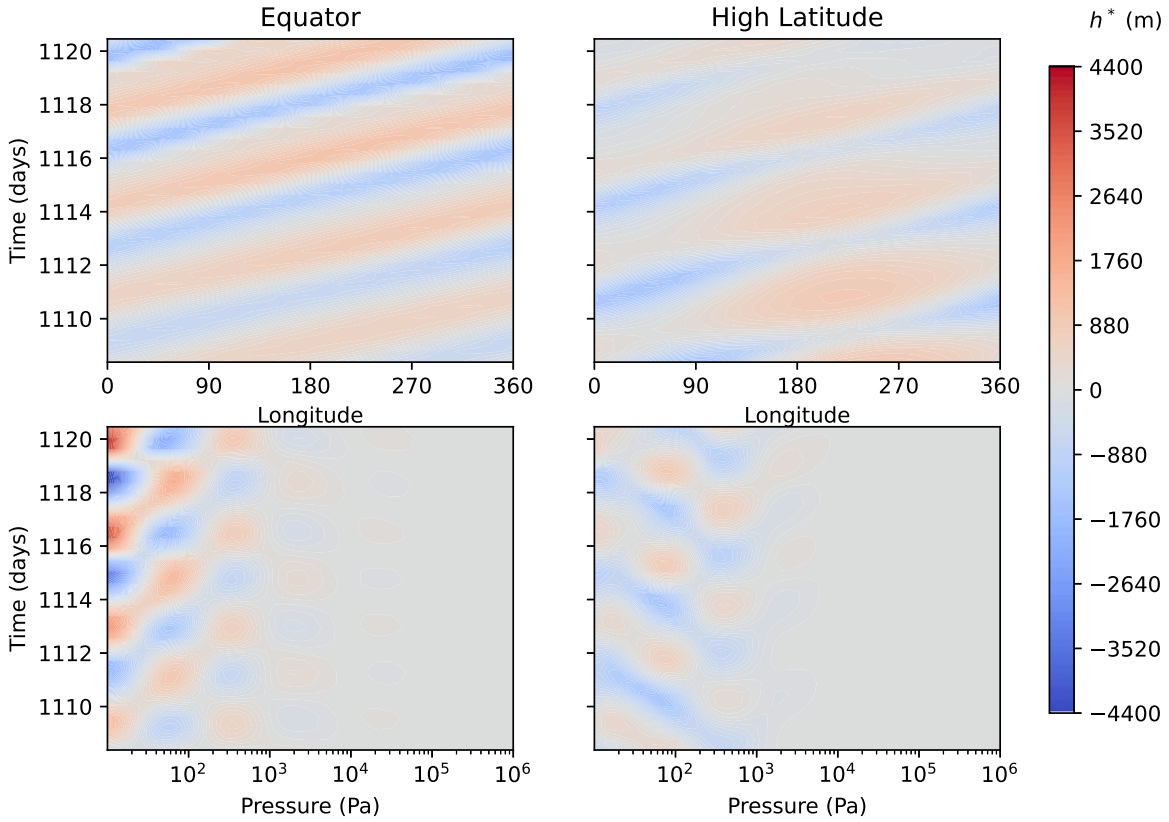


**Figure 14.** Hovmöller diagrams of the zonal-eddy height field, $h^*$, averaged over the equatorial region (left column) and high-latitude regions (i.e., 50°–80°, right column). Top row: there is a clear zonal wavenumber 1 wave in the height field propagating eastward. This structure is also clear at high latitudes; however, there is also some beating in the response. Bottom row: the vertical structure of the waves at the equator suggests that the waves may be standing in the vertical direction; however, the vertical structure at high latitudes is more complicated.

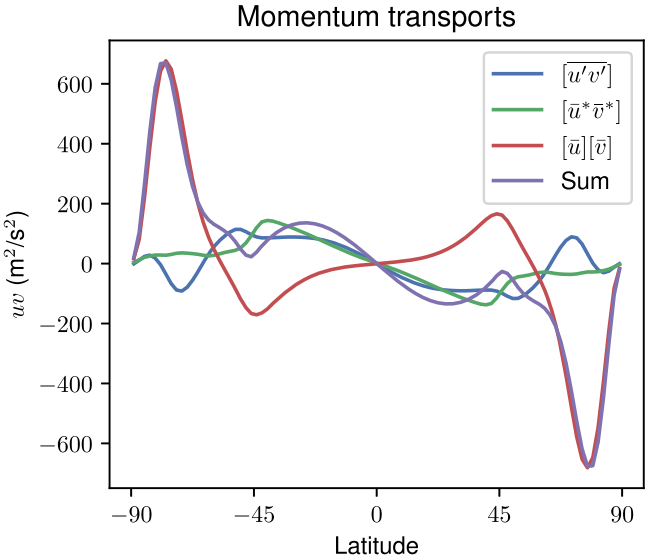


**Figure 15.** Terms in Equation (32) at the 40 Pa level. A negative gradient at the equator represents a convergence of eastwards momentum, causing an acceleration of the mean flow.

number of degrees of freedom), which in turn shortens the radiative timescale and can lead to higher day–night temperature contrasts.

The only other GCM study of K2-18b (Charnay et al. 2021; from now on referred to as C21) found a weak equatorial jet (speed around 50 m s$^{-1}$) at the 0.1–1 bar level and no high-latitude prograde jets for their solar-metallicity runs (which are most comparable to the PKc experiment in this paper). The atmosphere was dominated by the overturning circulation from day to night. This is in marked contrast to our simulations, where the strongest jets were high latitude, and the overturning day−night circulation, although being the dominant overturning circulation, was small in comparison to the rotational circulation. We find that the magnitude of equatorial jet speed at the level of heating (around 0.1 to 1 bar) in our PKc run (≈40 m s$^{-1}$) to be similar to the ≈50 m s$^{-1}$ strength equatorial jet in C21. A significant difference in the model of C21 is their inclusion of real-gas radiation, in comparison to our gray-gas scheme. This leads to a cooler troposphere in their model, along with larger vertical temperature gradients. One way this could influence the dynamics is in the setting of the Rossby radius, stated as

$$L_R = \sqrt{\frac{NH}{2\Omega}} \tag{33}$$

in C21, where $N \equiv \sqrt{g/T\,(g/c_p + dT/dz)}$ is the buoyancy frequency and $H$ the atmospheric scale height. We find that between 0.1 and 1 bars, C21 has vertical temperature gradients closer to adiabatic, leading to our value of $N$ being approximately 3 times larger than theirs, with relatively good agreement higher in the atmosphere. With a smaller $L_R$, Rossby waves are trapped closer to the equatorial region, and we would expect a stronger stationary-wave response, and perhaps a stronger jet. However, given the qualitative similarity between past studies using gray-gas and real-gas radiation

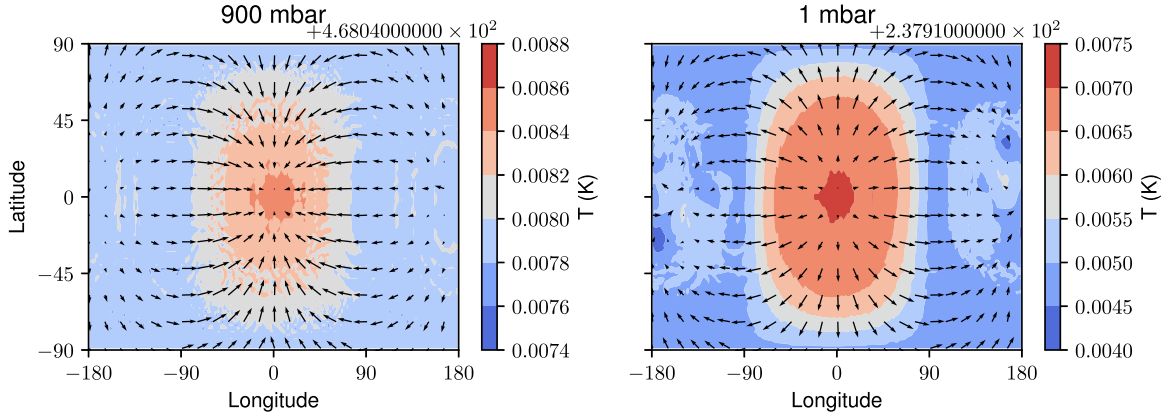


**Figure 16.** The temperature (contours) and wind fields (arrows) for the nonrotating model run. Left (1 bar level): isotropic convergence of wind at the substellar point and divergence at the antistellar point. Right (0.01 bar level): in the upper atmosphere the winds diverge around the substellar point and converge at the antistellar point.

(e.g., Kaspi & Showman 2015; Komacek & Abbot 2019; Lee et al. 2021), it would be surprising if the different radiation schemes accounted for all of the difference between the models. Other factors that could explain the disparity in wind structure include the type and strength of numerical damping schemes used and the type of dynamical core. ExoFMS uses a cubed-sphere grid, whereas the Laboratoire de Météorologie Dynamique's (LMD) generic GCM used in C21 uses a latitude–longitude grid, which could produce a variation between the models in the polar region where the latitude–longitude grid contains a singularity. The presence of high-latitude jets should be a robust result of transporting angular momentum from the equator to the poles, and our model should in theory produce less distortion at the poles due to the lack of coordinate singularity.

To test whether the poles are causing any distortion in the model, we ran the model with no rotation, which should in theory produce circulation symmetric around the substellar point. Figure 16 shows the temperature and wind fields in the lower and upper atmospheres, which exhibit the expected isotropic divergent flow around the substellar and antistellar point.

### 4.2. Validity of the Primitive Equations

In Mayne et al. (2019), the validity of using primitive equations for GCM simulations of hot super-Earths and sub-Neptunes was investigated. Simulations using the full Navier–Stokes equation in which $Z/a \geqslant 20\%$ (where $Z$ is the height of the dynamically active part of atmosphere and $a$ the planetary radius) begin to show significant deviations from the primitive equations due to the violation of the "shallow approximation." In our experiments, the maximum value of $Z/a$ was 8% for the two highest-instellation cases, justifying the use of the shallow approximation. We might expect this given our atmospheres are cooler than those in Mayne et al. (2019), with the scale height scaling with $T$. Mayne et al. (2019) also discuss the violation of the traditional approximation, where metric terms in the momentum equation become important. Similar to the method in Mayne et al. (2019), to check if $v\tan\phi \gg w$ (i.e., the traditional approximation is valid), we looked at the sign of $v\tan\phi/(10w) - 1$ at different pressure levels for each of our experiments. We found that $v\tan\phi \gg w$ in all experiments apart from a narrow narrow band at the equator (around $\pm 10°$ latitude), where $\tan\phi \ll 1$ and the traditional approximation is always invalid. As discussed in Mayne et al. (2019), if this region is limited and connected smoothly to the midlatitude flow, then the approximation is acceptable. With weaker radiative forcing than Mayne et al. (2019), we would expect $w$ to be smaller and therefore the traditional approximation is likely to be a good assumption in our experiments. Nonetheless, further investigation of the potential dynamical consequences of the nontraditional geometric terms for sub-Neptune atmospheres would be a fruitful subject for future investigation.

### 4.3. Scaling $\Lambda$ for General Sub-Neptunes

We now consider how the WTG parameter depends on stellar and planetary parameters to see if we can expect most temperate sub-Neptunes to have $\Lambda \gg 1$. If we use the equilibrium temperature $T_{\rm eq} \sim (S_0/\sigma)^{1/4}$ in estimating $\Lambda$, we note

$$S_0 = \frac{F}{4\pi d^2}, \tag{34}$$

where $F$ is the stellar luminosity and $d$ is the planet's orbital distance. Using Kepler's third law (note for a TL planet the orbital frequency is equal to the planet's rotation frequency):

$$d^2 = \left(\frac{GM_s}{\Omega^2}\right)^{\frac{2}{3}}, \tag{35}$$

where $M_s$ is the stellar mass, we find

$$S_0 = \frac{F}{4\pi G^{\frac{2}{3}}} M_s^{-\frac{2}{3}} \Omega^{\frac{4}{3}}. \tag{36}$$

If we are assuming $\Lambda = \sqrt{RT}/(\Omega a)$, this gives us an approximate scaling:

$$\Lambda \sim R^{\frac{1}{2}} F^{\frac{1}{8}} M_s^{-\frac{1}{12}} \Omega^{-\frac{5}{6}} a^{-1}. \tag{37}$$

We note that for M-type stars, $F$ varies from around $3 \times 10^{-4}\, L_\odot$ to 0.069 $L_\odot$ (making $(F_{\rm max}/F_{\rm min})^{1/8} \approx 2$), and $M_s$ varies from 0.08 to 0.57 $M_\odot$ (making $(M_{s,\rm max}/M_{s,\rm min})^{1/12} \approx 1.2$) (Pecaut & Mamajek 2013). If we restrict our focus to sub-Neptunes, $a$ varies from around 2 to 4 $R_\oplus$, i.e., by a factor of 2. Therefore, we expect that $\Lambda$ varies mostly due to the global rotation rate $\Omega$, and the composition $R \propto \mu^{-1}$, because $M_s^{-1/12}$ and $F^{1/8}$ do not vary

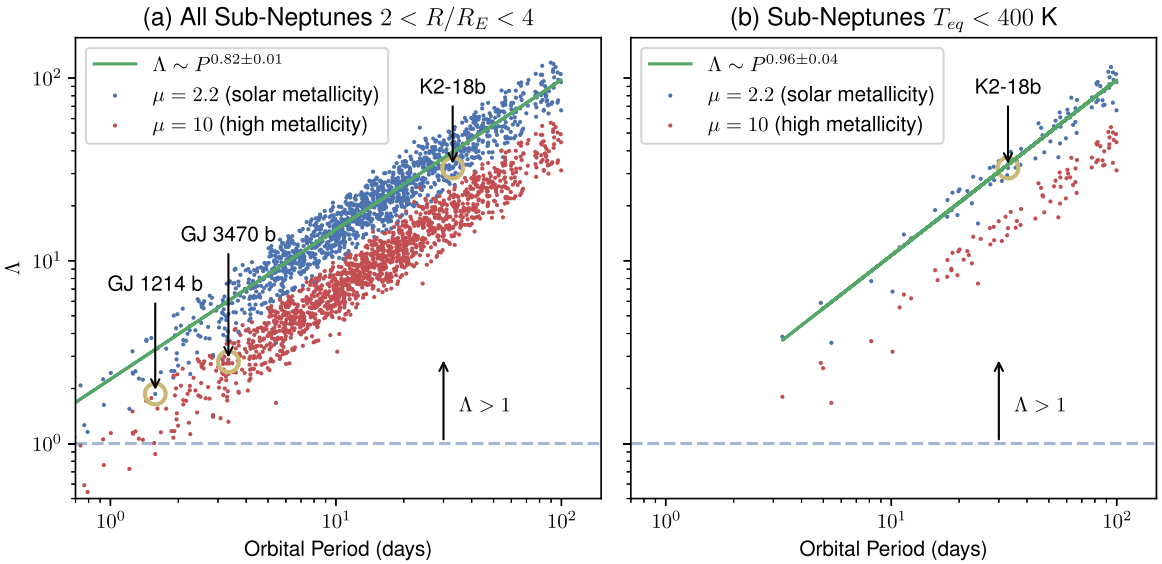


**Figure 17.** The weak temperature gradient parameter for observed sub-Neptunes with orbital period <100 days, assuming tidal locking. The blue data series assumes a mean molecular weight of 2.2 (see this study), whereas the red series has $\mu = 10$ to represent a higher metallicity atmosphere. (a) For all sub-Neptunes, we have $\Lambda > 1$ in the majority of cases, and that the scaling $\Lambda \sim P^{0.83} \approx P^{5/6}$ is in agreement with Equation (37), confirming that parameters $a$, $M_s^{1/12}$, and $F^{1/8}$ do not vary greatly over the range of sub-Neptunes. We also highlight the value of $\Lambda$ for three example sub-Neptunes (assuming $\mu = 2.2$). (b) Same as (a), but filtered for $T_{\rm eq} < 400$ K. Here $\Lambda > 1$ for all cases, but the scaling for $\Lambda$ is less accurate suggesting other parameters require scaling for.

significantly across the range of M-dwarf stars and $a^{-1}$ does not vary significantly for sub-Neptunes.

Figure 17(a) shows $\Lambda$ for all discovered sub-Neptune exoplanets with orbital period less than 100 days, assuming tidal locking.[2] We plot $\Lambda$ for low-metallicity ($\mu = 2.2$) and high-metallicity ($\mu = 10$) atmospheres and find that in both cases $\Lambda \gg 1$ for the majority of sub-Neptunes. The best-fit power law to the data also shows $\Lambda \sim P^{0.83\pm0.01}$, which is in agreement with Equation (37), and confirms the analysis that other parameters such as stellar mass and flux do not vary greatly over the range of sub-Neptune exoplanets.

We stress that having $\Lambda > 1$ does not imply that all planets in Figure 17(a) will exhibit weak horizontal temperature gradients. As discussed in Komacek & Showman (2016), Zhang & Showman (2017), and Section 3.2, temperature gradients also depend on the radiative timescale. Because $\tau_r \propto T^{-3} p(\tau = 1)$, planets with high equilibrium temperatures can have very short radiative timescales and will therefore exhibit strong day–night temperature contrasts. In addition, high-metallicity atmospheres where the level of radiative cooling, $p(\tau = 1)$, is high in the atmosphere due to increased LW opacity, will also have short radiative timescales. In Figure 17(b), we plot sub-Neptunes for which the equilibrium temperature, $T_{\rm eq}$, is less than 400 K. Here $\Lambda > 1$ always, and because $T$ is lower, we can be more confident these sub-Neptune atmospheres will have long radiative timescales similar to those in this study and exhibit similar dynamics to our simulated atmospheres.

### 4.4. 1D versus 3D Modeling

The magnitude of the horizontal temperature gradients provides a useful bound on the error of 1D column models of sub-Neptune atmospheres. For applications that do not depend on the structure of the 3D circulation (which is not horizontally uniform), 1D models may be able to give us useful insights at much lower computational expense than 3D GCMs. For our 33 day period experiments, the maximum fractional horizontal temperature difference from the substellar point (i.e., $(T - T_{\rm substellar})/T_{\rm substellar}$) is around 6%–8%, rising to 15%–22% in the 6 day period experiments. Whether this error is tolerable is context dependent. For example, in phase-curve calculations the projected area of the polar regions (where the temperature deviation from pure heat redistribution is greatest) is small and deviations may not affect calculations significantly. On the other hand, polar regions of the atmosphere would be important for transmission spectroscopy measurements.

Understanding the 3D structure of these atmospheres is crucial for some contexts. For example, estimates of the "$K_{zz}$" parameter in 1D chemistry models often rely on having information on the characteristic vertical velocities in an atmosphere (Zhang & Showman 2018). Because the vertical velocities in a GCM are controlled by the divergent circulation, scalings like Equation (26), which link the divergent circulation to planetary parameters, could be useful in estimating such quantities. Moreover, transport processes important in moving around chemical tracers and cloud particles are inherently 3D processes and so may not be amenable to simple 1D modeling. For example, C21 similarly found weak horizontal temperature gradients. However, the inhomogeneous circulation can cause spatially and temporally varying cloud profiles. Though we might expect the relative horizontal uniformity of temperature to survive inhomogeneous cloud effects, because it derives from the basic WTG scaling, cloud feedback could nonetheless have an important influence on the vertical structure of the atmosphere.

### 4.5. Model Limitations and Future Work

The gray-gas radiation used in our model is a crude approximation of the full radiative transfer calculation. As discussed in the introduction, we underestimate the temperature of the deep atmosphere by around 100 K compared to real-gas 1D simulations. Moreover, gray-gas atmospheres have a tendency to be subadiabatic throughout the atmosphere, underestimating the

[2] Data from the NASA Exoplanet Archive, https://exoplanetarchive.ipac.caltech.edu; accessed 2021 September 10.

value of the vertical temperature lapse rate. This is the same effect that led to our overestimation of $N$ compared to C21, though we note that in C21 the temperature profile is close to adiabatic in a very limited section of the atmosphere. However, the gray-gas scheme produces qualitatively similar temperature profiles to the real-gas models and should be valid for looking at global-scale circulations. Moreover, the gray-gas scheme is much less prohibitive in terms of its computational speed compared to using real-gas radiation, and allows us to run several comparative models of sub-Neptune atmospheres out to tens of thousands of days.

In this study we have examined the dry dynamics of the atmosphere to highlight the basic dynamical behavior. The tentative detection of water vapor in the atmosphere of K2-18b (Benneke et al. 2019b) and subsequent modeling (Blain et al. 2021; Charnay et al. 2021) have shown that there are circumstances under which water can condense in the atmospheres of sub-Neptunes. We will investigate the effect of condensation on the dynamics in Part II.

We would also encourage an intercomparison similar to the TRAPPIST Habitable Atmosphere Intercomparison project (Fauchez et al. 2021) to look at the differences between GCMs when modeling a fiducial sub-Neptune exoplanet. The difference between seemingly similarly setup GCM experiments (e.g., between ours and C21) suggests that further collaboration is required to illuminate the differences caused by different dynamical cores, physical parameterizations, and damping schemes. A good starting point would be an intercomparison between gray models, to highlight the dynamics.

Lastly, more work could be done on the instability found in the upper atmosphere to fully diagnose its origin and effect on the atmosphere, perhaps in the form of simplified models or instability analysis (e.g., Wang & Mitchell 2014).

## 5. Concluding Remarks

In this work we have presented a suite of GCM simulations aimed at modeling temperate sub-Neptune planets, using K2-18b as our control experiment. Overall these atmospheres exhibit weak horizontal temperature gradients. We found that these atmospheres are dominated by high-latitude cyclostrophic jets, with weak equatorial superrotation in the lower atmosphere and strong, instability-driven equatorial jets in the upper atmosphere. We confirmed the result of Wang & Wordsworth (2020), finding that our models have convergence times on the order of tens of thousands of days, increasing with slower rotation rate and lower instellation. We found that the high-latitude jets are cyclostrophically balanced in our fast-rotating experiment, with nonlinear advective terms providing a significant proportion of the balance in the slower-rotating, hotter experiments. Using the framework of Hammond & Lewis (2021), we decomposed the circulation into divergent and rotational components in TL coordinates, and found that although the dominant flow was rotational, the overturning circulation was dominated by a day–night circulation responsible for redistributing the energy deposited by instellation from the day side to the night side. We provided a scaling argument for how the strength of this circulation varies with instellation, finding that the TL stream function should scale as $S_0^{3/4}$.

In all our experiments, we observed equatorial superrotation in the upper atmosphere of our model, driven by an instability similar in structure to the one modeled in Wang & Mitchell (2014) to explain superrotation in slow, nonsynchronously rotating planets such as Venus and Titan. We showed that this instability occurred in the correct parameter regime as in Wang & Mitchell (2014) and that it provided eddy-momentum fluxes that could transport zonal momentum from the high-latitude jets toward the equator.

Finally, we compared our results to the literature, finding our results differ qualitatively to Charnay et al. (2021), who model K2-18b using the LMD Generic GCM but do not observe high-latitude cyclostrophic jets in their data. We offered some reasons why our model could produce different findings, but ultimately we recommend some form of intercomparison between GCM models to illuminate the effects of different physical parameterizations and dynamical cores on the atmospheres of sub-Neptunes. We noted the need to consider moist effects and leave that to the contents of a future study.

We thank Neil Lewis and Mark Hammond for letting us use their code to calculate Helmholtz decompositions and Neil Lewis, Shami Tsai, and Mark Hammond for useful discussions and comments on the manuscript. We thank the anonymous reviewer for their feedback, which improved this manuscript. This work was supported by grants from the European Research Council (Advanced grant EXOCONDENSE #740963 to R.T.P.)

*Software:* NUMPY (Harris et al. 2020), XARRAY (Hoyer & Hamman 2017), SCIPY (Virtanen et al. 2020), MATPLOTLIB (Hunter 2007), WINDSPHARM (Dawson 2016).

## Appendix A
## Effect of Pressure-dependent Short-wave Opacity

We present here a comparison of the P6c experiment (see Table 3) to an identical one run with the SW opacity proportional to $p$ (hereafter referred to as the pressure-dependent opacity (PDO) experiment). We changed the opacity such that the total SW optical depth of the atmosphere remained the same.

### A.1. Temperature Profiles

As shown in Figure 1, including pressure-dependent SW opacities increases the temperature at the bottom of the atmosphere. It also increases the pressure of the characteristic

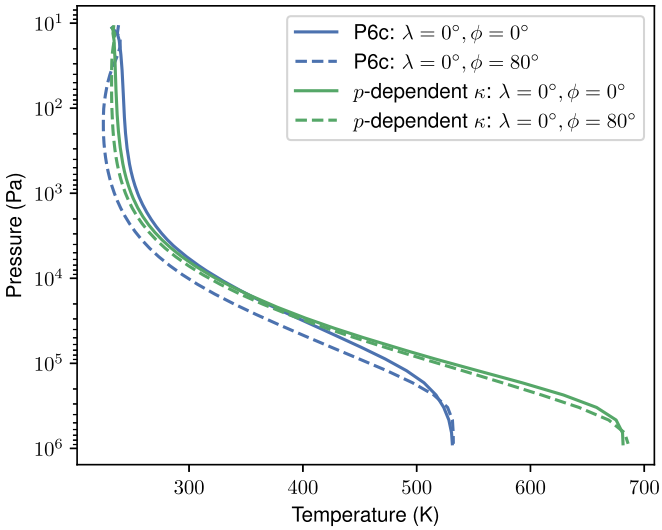


**Figure 18.** Latitudinal temperature variation of the two experiments. The case with pressure-dependent opacity shows a much smaller equator to pole temperature contrast.

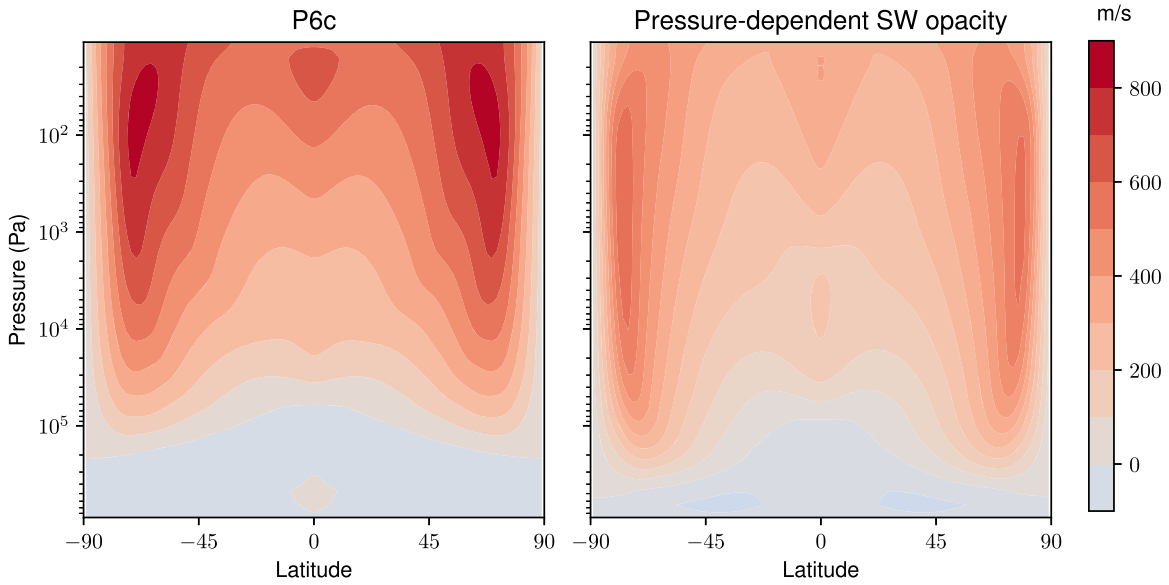


**Figure 19.** The zonal-mean zonal wind profiles.

SW heating level where $\tau_{SW} = 1$ by a factor of $\sqrt{\tau_{SW0}}$, where $\tau_{SW0}$ is the total SW optical depth of the atmosphere. In the context of our experiments, this moves the $\tau = 1$ level from 0.8 to 2.8 bar.

In Figure 18 we look at the latitudinal variation in temperature in both experiments. We note that the longitudinal variation at all latitudes is extremely small in both cases (on the order of $10^{-2}$ K). We see that the drop in temperature between the equator and pole is smaller in the PDO experiment, which confirms that we are still well within the weak temperature gradient regime discussed in the main text.

### *A.2. Zonal Wind*

In Figure 19 we compare the zonal-mean zonal wind profiles between the two experiments. The PDO experiment shows qualitatively similar zonal wind structure, with two high-latitude, cyclostrophically balanced zonal jets and equatorial superrotation with a maximum in the upper atmosphere. We note that the magnitude of the zonal wind in the PDO experiment is significantly lower than that in the P6c experiment, which is consistent with the lower equator-to-pole temperature difference seen in Appendix A.1 because this is proportional to the vertical wind shear in cyclostrophic balance. However, because we currently have no theory predicting the strength of this wind and temperature gradient a priori, we cannot explain why the magnitude of this wind differs on changing the SW heating profile.

We also note that the jets extend to higher pressures in the PDO experiment. This makes sense because the characteristic level of SW heating (discussed in Appendix A.1) is at a higher pressure in this experiment, which drives the dynamics at this level.

The instability discussed in Section 3.5 was also present in the PDO experiment.

### *A.3. Mass Stream Functions*

Lastly, we compare the mass stream functions of the two experiments (Figure 20). Qualitatively, the structure of the stream functions is similar between the two experiments. In the PDO runs, the level of the maximum stream function increases in pressure, which is linked once again to the characteristic level of SW heating moving to higher pressures. The magnitude of the TL stream function (which we related to the strength of the instellation in Section 3.4) is of the same order of magnitude but not identical between the two experiments. Our scaling in Section 3.4 linked the stream function to the magnitude of the solar heating. Because the maximum magnitude of the stream function is roughly at the level of characteristic SW heating in both cases (0.8 bar for P6c, 2.2 bar for PDO), we would expect the integrated heating at this level not to vary between cases. However, changes in the mean dry static energy and physics not accounted for by the crude approximations made in deriving the scaling law may cause the two values to be different.

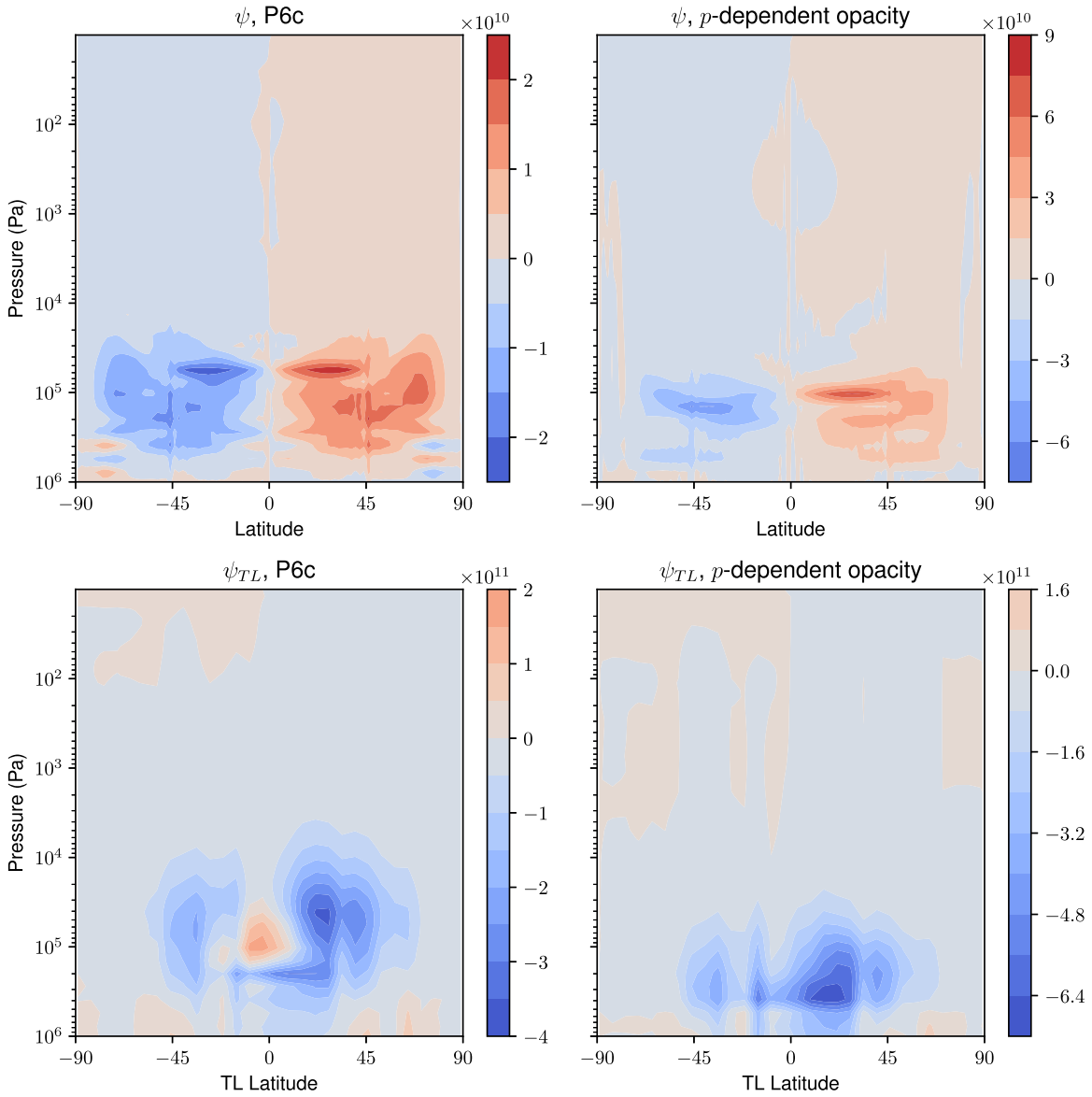


**Figure 20.** The mass stream function (in units of kg $s^{-1}$) in conventional latitude–longitude coordinates (top row) and tidally locked coordinates (bottom row) for the P6c (left) and PDO (right) experiments.

## Appendix B
## Temperature–pressure Profiles

We present in Figures 21 and 22 the temperature–pressure profiles of the noncontrol experiments (similar to Figure 4) for reference.

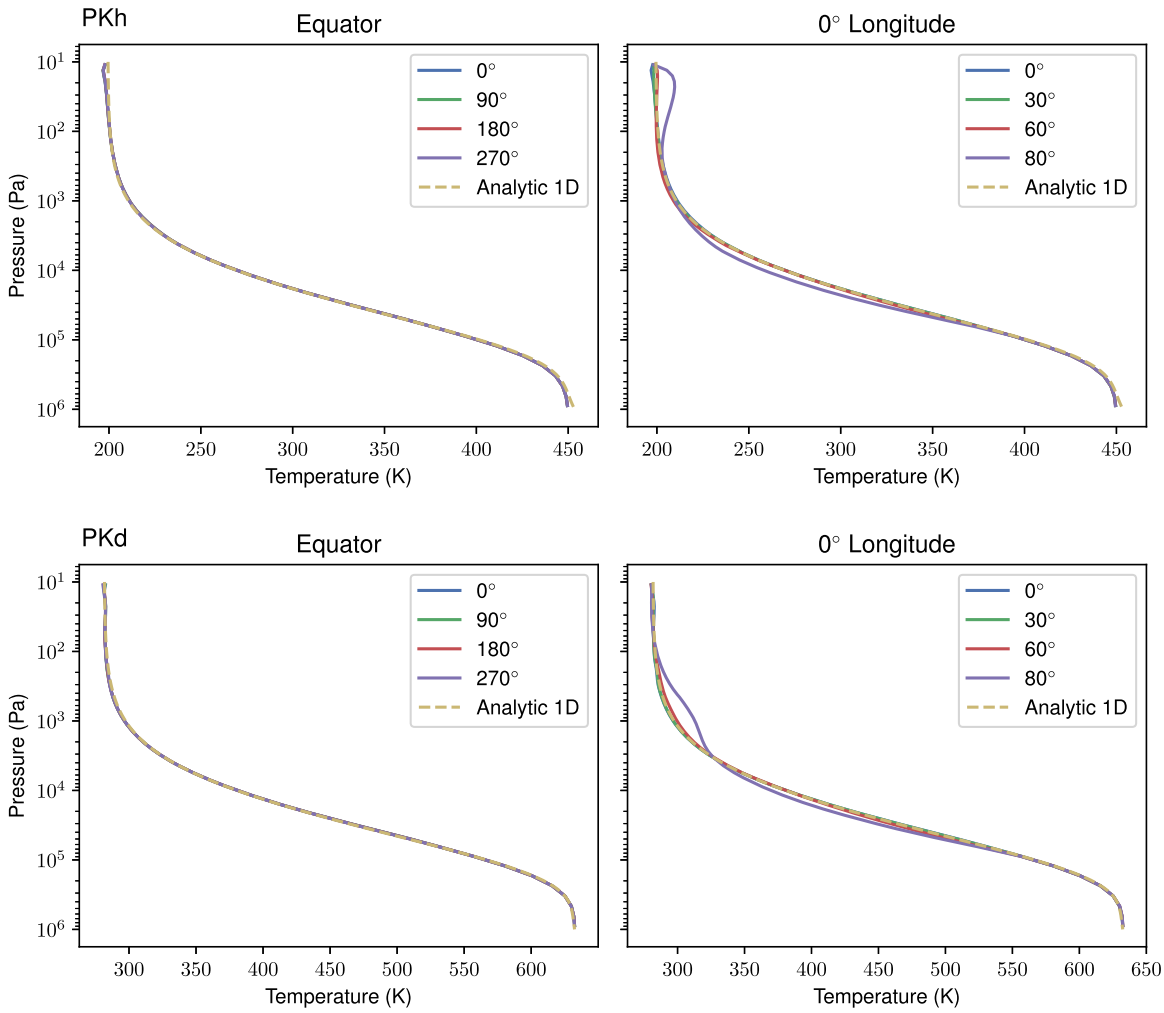


**Figure 21.** Temperature–pressure profiles of the noncontrol, 33 day period experiments.

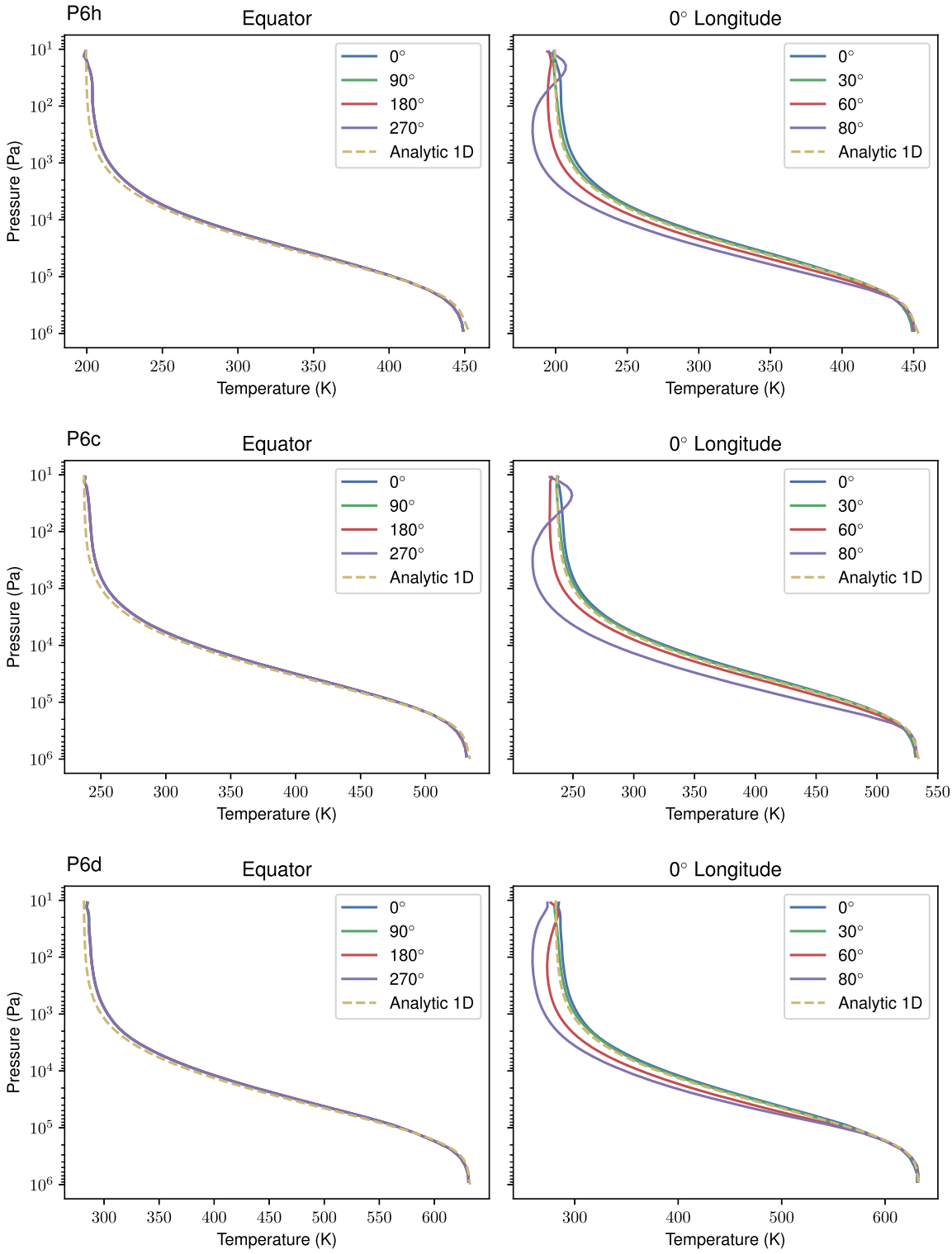


**Figure 22.** Temperature–pressure profiles of the noncontrol, 6 day period experiments.

## ORCID iDs

Hamish Innes https://orcid.org/0000-0001-5271-0635
Raymond T. Pierrehumbert https://orcid.org/0000-0002-5887-1197

## References

Batalha, N. M. 2014, PNAS, 111, 12647
Bean, J. L., Désert, J. M., Kabath, P., et al. 2011, ApJ, 743, 92
Benneke, B., Knutson, H. A., Lothringer, J., et al. 2019a, NatAs, 3, 813
Benneke, B., Wong, I., Piaulet, C., et al. 2019b, ApJ, 887, L14
Berta, Z. K., Charbonneau, D., Bean, J., et al. 2011, ApJ, 736, 12
Bézard, B., Charnay, B., & Blain, D. 2020, arXiv:2011.10424
Blain, D., Charnay, B., & Bézard, B. 2021, A&A, 646, A15
Casagrande, L., Flynn, C., & Bessell, M. 2008, MNRAS, 389, 585
Charnay, B., Blain, D., Bézard, B., et al. 2021, A&A, 646, A171
Charnay, B., Meadows, V., & Leconte, J. 2015a, ApJ, 813, 15
Charnay, B., Meadows, V., Misra, A., Leconte, J., & Arney, G. 2015b, ApJL, 813, L1
Cloutier, R., Astudillo-Defru, N., Doyon, R., et al. 2017, A&A, 608, A35
Cloutier, R., Astudillo-Defru, N., Doyon, R., et al. 2019, A&A, 621, A49
Dawson, A. 2016, JOSS, 4, 31
Dobbs-Dixon, I., & Agol, E. 2013, MNRAS, 435, 3159
Drummond, B., Mayne, N. J., Baraffe, I., et al. 2018, A&A, 612, 105
Fauchez, T. J., Turbet, M., Sergeev, D. E., et al. 2021, PSJ, 2, 106
Fortney, J. J., Mordasini, C., Nettelmann, N., et al. 2013, ApJ, 775, 80
Fulton, B. J., Petigura, E. A., Howard, A. W., et al. 2017, AJ, 154, 109
Gillon, M., Jehin, E., Lederer, S. M., et al. 2016, Natur, 533, 221
Ginzburg, S., Schlichting, H. E., & Sari, R. 2016, ApJ, 825, 29
Gupta, A., & Schlichting, H. E. 2019, MNRAS, 487, 24
Hammond, M., & Lewis, N. T. 2021, PNAS, 118, 2022705118
Hammond, M., & Pierrehumbert, R. T. 2017, ApJ, 849, 152
Hammond, M., & Pierrehumbert, R. T. 2018, ApJ, 869, 65
Hammond, M., Tsai, S. M., & Pierrehumbert, R. T. 2020, ApJ, 901, 78
Haqq-Misra, J., Wolf, E. T., Joshi, M., Zhang, X., & Kopparapu, R. K. 2018, ApJ, 852, 67
Harris, C. R., Millman, K. J., van der Walt, S. J., et al. 2020, Natur, 585, 357
Held, I. M., & Hou, A. Y. 1980, JAtS, 37, 515
Hoyer, S., & Hamman, J. J. 2017, JOSS, 5, 10
Hunter, J. D. 2007, CSE, 9, 90
Iga, S. I., & Matsuda, Y. 2005, JAtS, 62, 2514
Jablonowski, C., & Williamson, D. L. 2011, in Numerical Techniques for Global Atmospheric Models, ed. P. Lauritzen et al. (Berlin: Springer)
Kaspi, Y., & Showman, A. P. 2015, ApJ, 60, 804
Kataria, T., Showman, A. P., Fortney, J. J., Marley, M. S., & Freedman, R. S. 2014, ApJ, 92, 785
Kataria, T., Sing, D. K., Lewis, N. K., et al. 2016, ApJ, 821, 9
Kite, E. S., & Barnett, M. N. 2020, PNAS, 117, 18264
Kite, E. S., Fegley, B., Schaefer, L., & Ford, E. B. 2020, ApJ, 891, 111
Knutson, H. A., Dragomir, D., Kreidberg, L., et al. 2014, ApJ, 794, 55
Koll, D. D., & Abbot, D. S. 2015, ApJ, 802, 21
Koll, D. D. B., & Abbot, D. S. 2016, ApJ, 825, 99
Komacek, T. D., & Abbot, D. S. 2019, ApJ, 871, 245
Komacek, T. D., & Showman, A. P. 2016, ApJ, 821, 16
Kreidberg, L., Bean, J. L., Désert, J. M., et al. 2014, Natur, 505, 69
Leconte, J., Selsis, F., Hersant, F., & Guillot, T. 2017, A&A, 598, 98
Lee, E. K. H., Parmentier, V., Hammond, M., et al. 2021, MNRAS, 506, 2695
Lee, G. K., Casewell, S. L., Chubb, K. L., et al. 2020, MNRAS, 496, 4674
Lian, Y., & Showman, A. P. 2010, Icar, 207, 373
Lin, S. J. 2004, MWRv, 132, 2293
Lin, S. J., & Rood, R. B. 1997, QJRMS, 123, 2477
Liu, J., & Schneider, T. 2011, JAtS, 68, 2742
Lopez, E. D., & Fortney, J. J. 2013, ApJ, 2, 776
Madhusudhan, N., Nixon, M. C., Welbanks, L., Piette, A. A., & Booth, R. A. 2020, ApJL, 891, L7
Marcy, G. W., Weiss, L. M., Petigura, E. A., et al. 2014, PNAS, 111, 12655
Mayne, N. J., Debras, F., Baraffe, I., et al. 2017, A&A, 604, 79
Mayne, N. J., Drummond, B., Debras, F., et al. 2019, ApJ, 871, 56
Mayor, M., Marmier, M., Lovis, C., et al. 2008, A&A, 493, 639
Mendonça, J. M. 2020, MNRAS, 491, 1456
Menou, K. 2012, ApJL, 744, 16
Mikal-Evans, T., Crossfield, I. J., Benneke, B., et al. 2021, AJ, 161, 18
Mitchell, J. L., & Vallis, G. K. 2010, JGRE, 115, E12
Nettelmann, N., Fortney, J. J., Kramm, U., & Redmer, R. 2011, ApJ, 733, 2
Noda, S., Ishiwatari, M., Nakajima, K., et al. 2017, Icar, 282, 1
Owen, J. E., & Wu, Y. 2013, ApJ, 775, 105
Owen, J. E., & Wu, Y. 2017, ApJ, 847, 29
Pecaut, M. J., & Mamajek, E. E. 2013, ApJS, 208, 9
Perez-Becker, D., & Showman, A. P. 2013, ApJ, 776, 134
Petigura, E. A., Howard, A. W., & Marcy, G. W. 2013, PNAS, 110, 19273
Pierrehumbert, R. T. 2010, Principles of Planetary Climate (Cambridge: Cambridge Univ. Press)
Pierrehumbert, R. T., & Ding, F. 2016, RSPSA, 472, 20160107
Pierrehumbert, R. T., & Hammond, M. 2019, AnRFM, 51, 275
Piette, A. A., & Madhusudhan, N. 2020, ApJ, 904, 154
Putman, W. M., & Lin, S. J. 2007, JCoPh, 227, 55
Rajpurohit, A. S., Reylé, C., Allard, F., et al. 2013, A&A, 556, 15
Rauscher, E., & Kempton, E. M. 2014, ApJ, 790, 79
Rauscher, E., & Menou, K. 2010, ApJ, 714, 1334
Rogers, L. A., & Seager, S. 2010, ApJ, 716, 1208
Scheucher, M., Wunderlich, F., Grenfell, J. L., et al. 2020, ApJ, 898, 44
Sergeev, D. E., Lambert, F. H., Mayne, N. J., et al. 2020, ApJ, 894, 84
Shaw, T. A., & Shepherd, T. G. 2007, Journal of the Atmospheric Sciences, 64, 190
Showman, A. P., & Guillot, T. 2002, A&A, 385, 166
Showman, A. P., Lewis, N. K., & Fortney, J. J. 2015, ApJ, 801, 95
Showman, A. P., & Polvani, L. M. 2011, ApJ, 738, 71
Tsai, S. M., Dobbs-Dixon, I., & Gu, P. G. 2014, ApJ, 793, 141
Tsiaras, A., Waldmann, I. P., Tinetti, G., Tennyson, J., & Yurchenko, S. N. 2019, NatAs, 3, 1086
Vallis, G. K. 2017, Atmospheric and Oceanic Fluid Dynamics: Fundamentals and Large-Scale Circulation (2nd edn.; Cambridge: Cambridge Univ. Press),
Virtanen, P., Gommers, R., Oliphant, T. E., et al. 2020, NatMe, 17, 261
Wang, H., & Wordsworth, R. 2020, ApJ, 891, 7
Wang, P., & Mitchell, J. L. 2014, GeoRL, 41, 4118
Winn, J. N., & Fabrycky, D. C. 2015, ARA&A, 53, 409
Yang, J., Boué, G., Fabrycky, D. C., & Abbot, D. S. 2014, ApJL, 787, L2
Zhang, X., & Showman, A. P. 2017, ApJ, 836, 73
Zhang, X., & Showman, A. P. 2018, ApJ, 866, 2